Information Technology for Manufacturing Systems IV

Edited by
Wei Deng and Qi Luo

TRANS TECH PUBLICATIONS

Information Technology for Manufacturing Systems IV

Edited by
Wei Deng
Qi Luo

Information Technology for Manufacturing Systems IV

Selected, peer reviewed papers from the
2013 4th International Conference on
Information Technology for Manufacturing Systems
(ITMS2013),
August 28-29, 2013, Auckland, New Zealand

Edited by

Wei Deng and Qi Luo

Trans Tech Publications Ltd
Kreuzstrasse 10
CH-8635 Durnten-Zurich
Switzerland
http://www.ttp.net

Volume 421 of
Applied Mechanics and Materials
ISSN print 1660-9336
ISSN cd 1660-9336
ISSN web 1662-7482

Full text available online at *http://www.scientific.net*

***Distributed** worldwide by*

Trans Tech Publications Ltd
Kreuzstrasse 10
CH-8635 Durnten-Zurich
Switzerland

Fax: +41 (44) 922 10 33
e-mail: sales@ttp.net

and in the Americas by

Trans Tech Publications Inc.
PO Box 699, May Street
Enfield, NH 03748
USA

Phone: +1 (603) 632-7377
Fax: +1 (603) 632-5611
e-mail: sales-usa@ttp.net

Preface

Extended and revised versions of reviewed papers are included from 2013 4th International Conference on Information Technology for Manufacturing Systems (ITMS 2013) will be held on August 28-29,2013, Auckland, New Zealand . ITMS 2013 is sponsored by Singapore Management And Sports Science Institute, Singapore

ITMS 2013 will be the most comprehensive Conference focused on the various aspects of advances in Information Technology for Manufacturing Systems. Being crucial for the development of Industry, Manufacture and Materials, our conference encompasses a large number of research topics and applications: from Industry to many kinds of new Materials; from Material Science to Engineering Materials and other related topics are included in the scope of this conference. In order to ensure high-quality of our international conference, we have high-quality reviewing course, our reviewing experts are from home and abroad and low-quality papers have been refused.

For this special issue about 370 manuscripts were presented and 167 were selected for publication and can be classified into 6 chapters namely 1) Mechanical Engineering 2) Industry and Manufacture 3) Chemistry, Chemical Industry and Biological materials 4) Computer and Information Technology 5) Architecture and Civil Engineering 6) Environmental Engineering and Energy Engineering.

The papers under chapter 1 primarily introduced theory and application of kinds of mechanical engineering. The papers under chapter 2 showed us lots of recently research achievements in industry and manufacture field. The papers under chapter 3 to 6 mainly focus on the chemistry, chemical industry and biological materials, computer and information technology, architecture and civil engineering and environmental engineering and energy engineering

Noting can be done without the help of the program chairs, organization staff, and the members of the program committees. Special thanks go to TTP Publisher.

The goal of this Conference is to bring together the researchers from academia and industry as well as practitioners to share ideas, problems and solutions relating to the multifaceted aspects of Information Technology for Manufacturing Systems. In addition, the conference organizer will invite some famous keynote speaker to deliver their speech in the conference. All participants have chance to discuss with the speaker face to face, which is very helpful for participants. We are confident that the conference program will give you detailed insight into the new trends. We hope that ITMS 2013 will be successful. Next year, in 2014, we look forward to seeing all of you at ITMS2014.

Wei Deng and Qi Luo

ITMS 2013 Organizing Committee

Keynote Speaker and Honorary Chairman

Jun Wang, The Chinese University of Hong Kong, Hong Kong
Gerald Schaefer, Loughborough University, U.K
Chin-Chen Chang, Feng Chia University , Taiwan

General Chairs

Min Wu, Nanchang University, China
Wei Lee, Asia Pacific Human- Computer Interaction Research Center, Hong Kong

Program Chairs

Yiyi Zhouzhou, Azerbaijan State Oil Academy, Azerbaijan
Riza Esa, Kuala Lumpur ACM Chapter, Malaysia
Xiang Lee, Hong Kong Education Society, Hong Kong

Publication Chairs

Wei Deng, American Applied Sciences Research Institute, USA
Qi Luo, Singapore Management and Sports Science Institute, Singapore

Program Members

Jiang Chi, Peking University, China
Yu Tian, Anyang Normal University, China
Yijin Wu, Huazhong Normal University, China
Zhongming Yao, Qiqihar University, China
Yun Zhang, Southwestern University of Finance and Economics, China
Xiaolan Liu, Beijing Normal University, China
Wang Jianfen, Jiangsu Universty, China
Jinzhuo Liu, Henan University, China
Wang Yunyin, XinJiang University, China
Wang Zhonghua, Hubei University, China
Tatsuya Akutsu, ACM NUS Singapore Chapter, Singapore
Yiyi Zhouzhou, Azerbaijan State Oil Academy, Azerbaijan
Khine Soe Thaung, Maldives College of Higher Education, Maldives
Biswanath Vokkarane, Society on Social Implications of Technology and Engineering, Maldives

Table of Contents

Chapter 1: Research and Design of Machine Parts and Mechanisms for Manufacturing Systems

Chapter 2: Materials Science, Microbiology, Chemical Engineering and Technologies of Materials Exploration and Processing

Chapter 3: Technologies of Measurement, Monitoring and Detection

Chapter 6: Computer, Communication and Information Technologies

Chapter 7: Architecture and Civil Engineering

Chapter 8: Environmental Engineering

Chapter 9: Engineering Management

CHAPTER 1:

Research and Design of Machine Parts and Mechanisms for Manufacturing Systems

Applied Mechanics and Materials *Online: 2013-09-11*
ISSN: 1662-7482, Vol. 421, pp 3-9
doi:10.4028/www.scientific.net/AMM.421.3

A Study of Wind Heating System

T.C. Li[1, a], H.W. Wu[2,b]

[1]Department of Mechanical and Computer-Aided Engineering, St. John's University, 499, Sec. 4, Tam King Road, Tamsui District, New Taipei City 251, Taiwan, R.O.C.

[2]Department of Mechanical Engineering, Nan Jeon Institute of Technology, No.178, Chaoqin Road, Yanshui District, Tainan City 73746, Taiwan, R.O.C.

[a]li@mail.sju.edu.tw, [b]whwu@mail.njtc.edu.tw

Keywords: Solid friction; Wind heating; Heat transfer

Abstract. At present, the world is facing energy shortage, while the CO_2 emitted from the combustion of traditional energy causes greenhouse effect. As a result, the green concept of energy saving has emerged. Among the current green energies, solar power is not cost effective, and wind energy has great potential in terms of cost and efficiency. Most of wind energy is used for wind power generation, however, the wind energy is also applicable to heating, and the generated heat energy can be used for hot water supply and temperature regulation. The wind heating modes include fluid mixing and solid friction modes. This study used natural wind to design a machine producing heat energy by solid friction. The energy transfer mode of the wind heating system was to convert the blade extracted wind energy into mechanical energy, and use friction to generate mechanical energy generates. The heat energy was transferred to the water through heat exchange to increase the water temperature. The friction mode was to rub the brake pad against the disc to produce heat, and using the compression spring to adjust the magnitude of the friction. The pump circulated water to implement forced convection, and the heat exchange was designed as flowing water channel increasing the heat transfer time. The experimental results showed that the water storage temperature can be increased.

Introduction

In recent years, facing the environmental issues of greenhouse effect and rapid retreating of arctic ice, the green concept of energy saving has emerged. In Taiwan, the ratio of using solar water heaters in the south area, where the sunlight period is long during the summer, has increased. The solar collector can absorb solar radiation energy to heat the water in the tank, making the solar water heater a worthwhile long-term investment. However, the sunlight period during winter is short, thus greatly reducing the efficiency of the water heater, which people rely on during cold air season. Therefore, how to utilize the winter monsoon to produce heat energy is worth studying. Wind velocity can be accurately measured using the anemoscope. The wind velocity is expressed in m/sec or Beaufort wind scale [1]. The current use of wind power include water pumping, wind aided navigation, wind power generation, and wind heating. Therefore, this study used the cold wind in the winter season to generate heat energy.

Experimental system architecture and analysis

The wind heating modes include: 1) mixing: using wind turbine to drive mechanical energy to generate heat energy; 2) combination of wind power generation and solar energy; 3) heat pump: using wind turbine to drive compressor to generate heat energy and friction and so on. This study used solid friction to generate heat energy, and used the brake pad and disc for braking as friction materials. Past studies have suggested that the brake pad and disc do not have heat reduction problem at a high temperature. The principle of the experimental machine is to use wind to drive the wind turbine blades for rotation. Eq. 1 is used to calculate the power, which is influenced by frictional force and friction rotation diameter. The wind heating system was designed considering the two influencing factors. The wind turbine drives the brake pad directly to rotate and rub against the disc. The generated heat energy is then transferred by heat exchanger to the water to increase the water temperature. The density is 1 when the water temperature is 4℃. The density decreases as the temperature rises, so the natural circulation is also known as natural convection. In order to increase the friction force, the compression spring was used to increase the friction between brake pad and disc. The transfer process of wind-induced heat energy was converting the blade extracted wind energy into mechanical energy, and using friction to drive the mechanical energy to generate heat. The heat energy was then transferred to the water by heat exchange to increase the water temperature. The forced circulation architecture is shown in Figure 1. The forced circulation design is shown in Figure 2.

$$P = F_k \times S \tag{1}$$

P : heat power (W/min)

F_k : magnitude of friction (kg)

S : traveling distance per minute (mm/min)

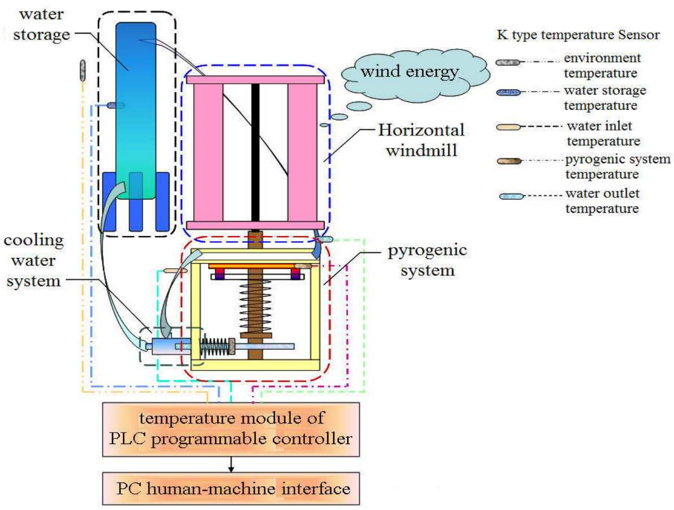

Figure 1 Composition position of the pyrogenic system

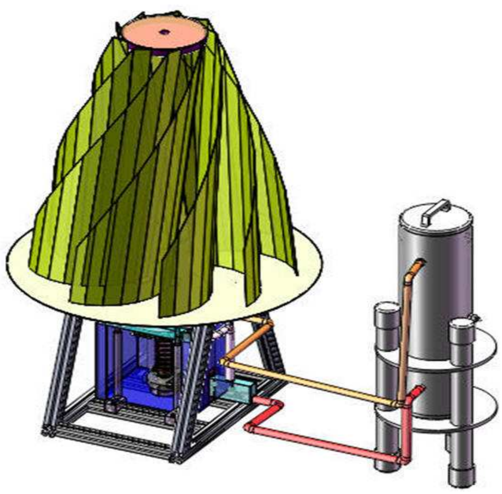

Figure 2 Layout of 3D diagram

Wind turbine system

There are two types of wind turbines according to the blade rotation mode: (1) horizontal axis wind turbine (HAWT): the rotation axis is parallel to the wind direction; (2) vertical axis wind turbine (VAWT): the rotation axis is vertical to the wind direction. According to the properties of the blades, the two axis wind turbines can be divided into resistive and lifting blades. This study used vertical axis blades to drive the axis rotation and the heating system, as the vertical axis is characterized by low wind velocity and high torsion [3][4]. A closed nine-blade taper was used as the blades of this machine to extract wind energy. The closed nine-blade taper could be started up when the load is large. The size was 80cm, and the wind area was 3.6m^2. The schematic diagram and stereogram of the closed nine-blade taper are shown in Figure 3.

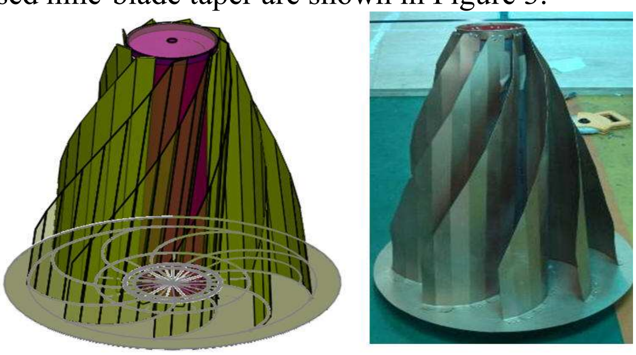

Figure 3 Schematic diagram of nine blades sharp closed cone type and photo of actual object

Wind turbine extracts wind to drive mechanical energy. The mechanical energy is converted into kinetic energy, and the kinetic energy contributes to the friction between brake pad and disc to generate heat energy. The wind turbine drives the main shaft to rotate and the ram drives the brake pad to rub against the disc to generate heat energy, Figure 4 shows the traveling distance of brake pad and disc when the wind turbine rotates. The traveling distance of single brake pad is calculated as Eq. 2.

$$S = \omega \times \pi \times D \quad (2)$$

S : traveling distance per minute (mm/min)
D : diameter of center rotation (mm)
ω : rotation speed (rev/min)

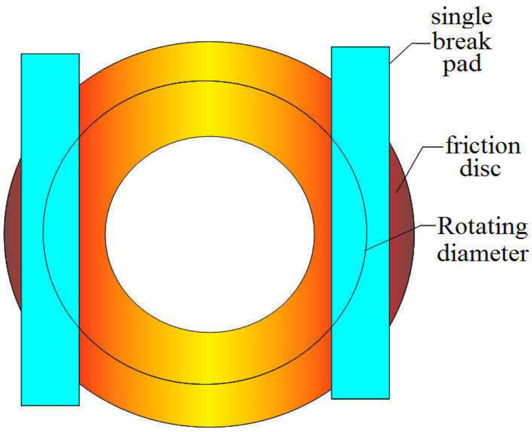

Figure 4 Schematic diagram of single break pad displacement

Circulation system

The proposed system actuates a pump to pump the low temperature water from the water storage tank into the flowing water channel for heat exchange in order to heat the water. The axle center rotates driving the eccentric wheel, so that the piston rod and compression spring move forward and backward to pump and squeeze water. The pumping scheme is shown in Figure 5. The water flow supplied by each actuation is calculated as Eq. 3.

$$Q = \frac{1}{4} \times \pi \times d^2 \times 2e \times \omega \quad (3)$$

Q : flow rate (mm^3/min)
d : radius of piston rod (mm)
e : stroke of piston rod (mm)
ω : rotation speed (rev/min)
* Radius of piston rod d=8.25mm, stroke of piston rod e=12.5mm

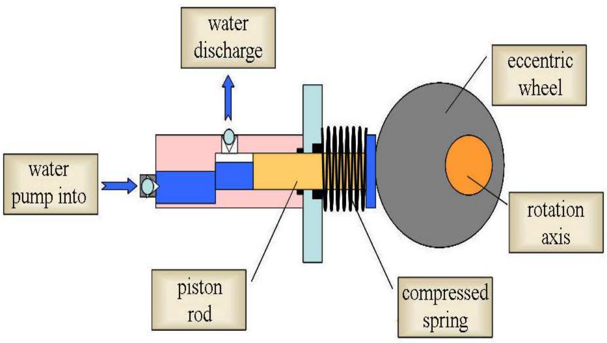

Figure 5 Schematic diagram of pump

Heating system design

The proposed heating system design generates heat energy by solid friction, the compression spring increases the resistance of solid friction, so that the friction temperature increases rapidly to generate the required heat energy. The heat energy is transferred downward through fins to the water for heat exchange effect. The obtained heat energy is preserved by heat insulated cotton to reduce the dissipation of heat energy.

Heat exchange system

In the heat-exchanging system, the heat energy generated by the friction between brake pad and disc is transferred to the aluminum block. A water channel is hollowed in the middle of aluminum block, so that the water extruded by the pump flows through the water channel to absorb heat energy. The water flowing process and the flow channel design are shown in Figure 6. The heat-exchanging system consists of a square aluminum block drilled four holes and aluminum blocks on both sides, which are processed and combined with the square aluminum block. As the design generates heat by water flow channel, the joint is designed with rubber ring for waterproof. A temperature sensor is mounted to measure the curve of changes in water temperature after heat exchange. The volume of flowing water channel is 12.9cm^3 as calculated by Eq. 4.

$$V=\pi \times r^2 \times L \tag{4}$$

V: volume of flowing water channel (mm^3)
r: radius of flowing water channel (mm)
L: length of flowing water channel (mm)
* Radius of flowing water channel r=6.5mm,
Length of flowing water channel L=970mm
* Volume of water channel V=128685.05mm^3 =129cm^3

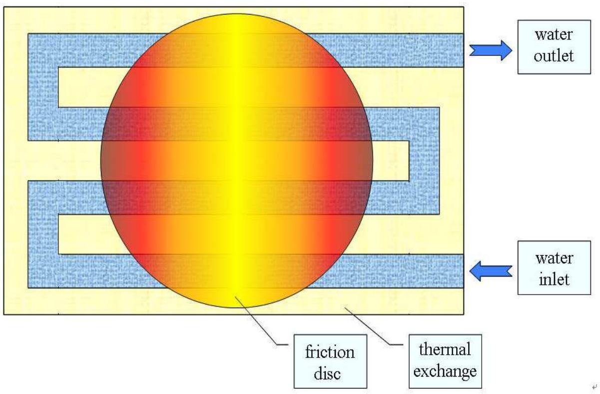

Figure 6 Schematic diagram of the cooling water flow channel designed

Compression spring

As the upward transfer of heat is fast, the friction device is fixed to the bottom of heat exchange, as shown in Figure 7. The data in Table 1 are substituted in Eq. 5 to obtain the spring coefficient k=0.195 kg/mm. The overall length of compression spring is 139mm, but the loaded brake pad and ram weight is 0.79kg at the beginning. Thus, the length of compression spring on the machine is 135mm, and the overall length of direct compression spring is set as 135mm for calculation. The force applied to the disc is calculated by Eq. 6. The deflection of the spring is 0~25mm, the spring force is 0~4.9kg, and the force applied to the disc is 0~2kg as calculated by Eq. 7.

Table 1 Data of spring

full-length of spring (mm)	spring force (Kg)	compressive displacement (mm)
139	0.79	4

$$F = k \times (L-X) \tag{5}$$

F : output force of compression spring (kg)
k : spring coefficient (kg/mm)
L : overall length of spring (mm)
X : length of spring after deflection (mm)

$$F_k = \mu_k \times (F\text{--}w) \tag{6}$$

F_k : force applied to disc (kg)
μ_k : kinetic friction coefficient
F : output force of compression spring (kg)
w : deadweight of disc (kg)

$$F_k = \mu_k \times F \tag{7}$$

F_k : force applied to disc (kg)
μ_k : kinetic friction coefficient

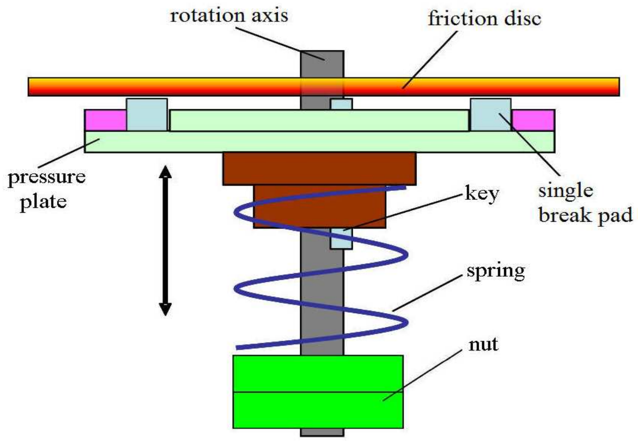

Figure 7 Schematic diagram of the compression spring displacement

Data acquisition design

The heating effect of the wind heating system should be known, therefore, the K Type temperature probe is mounted to measure the temperature change. The programmable controller Fatek PLC expansion temperature module was used to store the temperature measured by K Type temperature probe, and the PC man-machine interface read the measured value of temperature directly. The temperature probes measured the temperature changes in heating system, heat exchanger, tank and ambient.

Experimental data analysis

The heat energy is generated by solid friction driven by wind power, and the heat is transferred by heat exchange to the water to increase the water temperature. As the weather changes throughout the day, the wind velocity changes, thus influencing the wind turbine speed. The rotation cannot be maintained at a constant speed to drive solid friction to generate heat energy. In order to maintain the rotating speed, a three-phase induction motor was used to drive mechanical energy for solid friction to generate heat energy. The frequency converter controlled the induction motor speed. The proposed system was designed as forced circulation. Eq. 1 shows the traveling distance and friction influence the power.

Actual test for fan

Fan and frequency converter were used to find out the performance. A frequency converter controlled fan was used to supply the wind for test. Figure 8 shows the curve diagram of frequency and wind velocity. The data were measured with one meter in front of the fan. The closed nine-blade taper was fixed to the machine to test whether this machine could generate heat energy.

The forced circulation was tested with the upper force of compression spring and pump force. The startup failed in limiting conditions, so it rotated when the pump was removed. Figure 9 shows the rotation speed without load. Figure 10 shows the rotation speed when the amount of spring compression is 10mm. Figure 11 shows the fan blowing the proposed system for 4 hours. The brake pad was worn and abraded after long-term experiment. The temperature dropped as the ejection force changes. The test site was in the machine shop, and the test was performed from 9~10 a.m. to 12~1 p.m. The ambient temperature increased with the temperature inside the plant at about noontime.

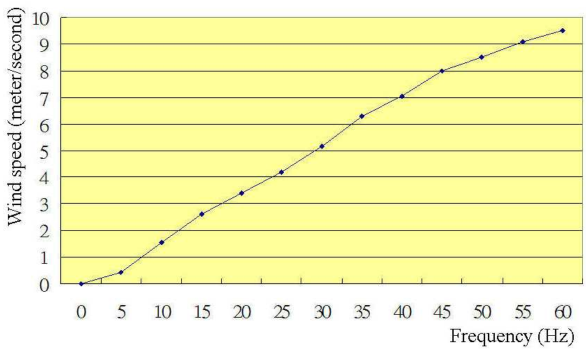

Figure 8 Graph of the wind speed and frequency

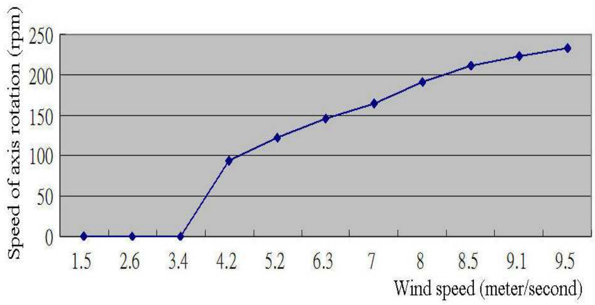

Figure 9 Speed of rotation axis at un-load case

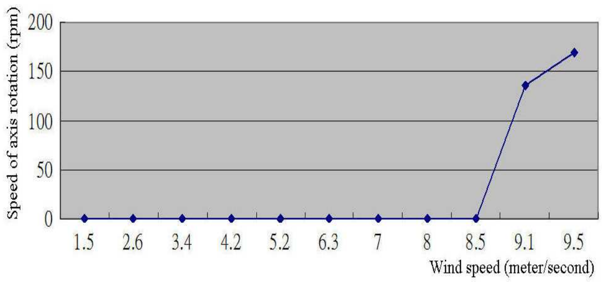

Figure 10 Speed of axis rotation of the spring was compressed 10 mm

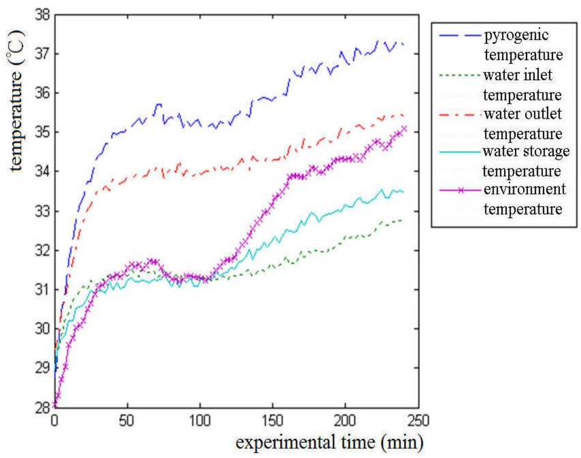

Figure 11 Operating temperature curve of measurement position of pyrogenic system by Industrial fan blowing directly for four hours

Conclusions and Suggestions

Conclusions

(1) The forced circulation design increased the flow of water, the repeated actuation of pump pumps and extrudes water. The low temperature water in the water storage cylinder could be pumped and extruded into the heat exchange effectively for heat transfer. When the wind turbine speed increased, the pump actuation frequency increased, and the water flew faster.

(2) The heat exchanger was designed as an aluminum block hollowed four water channels, so that the water flew through smoothly and the water staying time increased to absorb heat energy for heat transfer.

(3) The down pressure and rotation speed of compression spring could influence the heat transfer rate. When the temperature difference was large, the heat transfer rate was high, and the saturated phenomenon was reached.

Suggestions

(1) The power influencing parameters are the magnitude of friction and the traveling distance. The two parameters are adjusted by optimization, the optimized design can be obtained.

(2) The solid friction generates resistance which may cause abrasion and wear. The heat energy is generated by non-contact, thus the resistance and abrasion of objects can be reduced, without inconsistent force resulted from friction.

References

[1] http://140.127.114.16/energyworld/powerworld /main/chap04-topics/1.reports/EA/wind/3.htm.

[2] http://hk.geocities.com/ccfyt/meteotbl.htm.

[3] Chen, C.H., "A Study of Design of Blades Efficiently Extracting Wind Energy for Vertical Axis Wind Turbine Power Generation System", June 2004, Mingdao University.

[4] Sun, Y., "Design and Implementation of New Type of Vertical Axis Wind Turbine Power Generation System", June 2007, Department of Electrical Engineering, Tamkang University.

Applied Mechanics and Materials
ISSN: 1662-7482, Vol. 421, pp 10-15
doi:10.4028/www.scientific.net/AMM.421.10

Online: 2013-09-11

Research on the Space Meshing Tooth Profile of Giant Magnetostrictive Harmonic Motor *

Lin-jian Zhu[a],Zeng-rong Su, Zhen Zou, Jian-feng Li

School of Mechanical Engineering, Dalian University of Technology, Dalian 116024, China

[a]Email Address: zlj@dlut.edu.cn

Keywords: Conjugate Tooth Profile; Deformation Function; Equal Width Shrinkage; Harmonic Drive.

Abstract. A methodology to calculate the meshing tooth of giant magnetostrictive harmonic motor is proposed in this paper. The deformation curve of the flex spline of the giant magnetostrictive harmonic motor was investigated with Fourier function. A kinematic model of harmonic drive was established when the involute profile is selected as the flexible gear tooth shape and the circular spline is obtained following the envelope theory, thereby generating the kinematic simulation as well as the trajectory of the circular spline teeth with respect to the flex spline. Finally, the relationship between the cone angle of flex spline and the engagement profile is discussed; together with an improvement strategy- equal width shrinkage of circular spline.

Introduction

The advantage of harmonic drive include: no backlash, compactness and light weight, high gear ratios, good resolution and excellent repeatability. It has now been applied in aerospace, robotics, and other area. The giant magnetostrictive harmonic motor discussed in this paper is made from Giant Magnetostrictive Material (GMM), which is able to drive the flex spline to generate radial deformation directly for the ease of a drive unit with low velocity and high torque [1].

The working principle of GMM harmonic motor is shown in Fig. 1. The wave generator and the flex spline is the input rotation while the circular spline is the output rotation. The wave generator consists of eight drives which are uniformly distributed along the circumferential direction. Each drive contains a GMM actuator and a Hydraulic Micro-displacement Amplifier (HMA). In each drive, the drive coil is energized producing a magnetic field to drive the GMM rod with an axial micro-displacement which leads to a same axial displacement of the HMA input piston. When an axial displacement is generated in the input piston, it is transmitted to the mandrel through the working medium in the closed cavity. The displacement ratio between the output displacement and the input one is the ratio between the cross-sectional area of the input piston and that of the mandrel. Therefore, the output displacement can be changed by adjusting the current size of the driver coil.

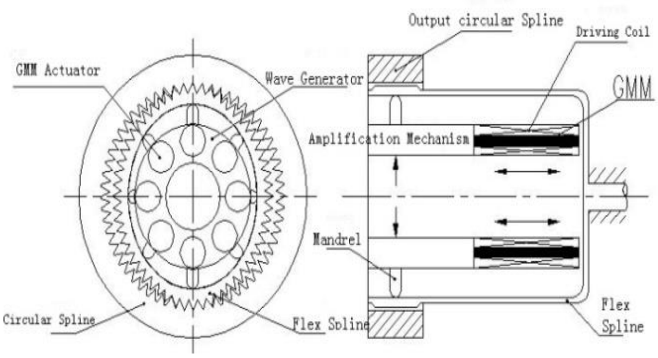

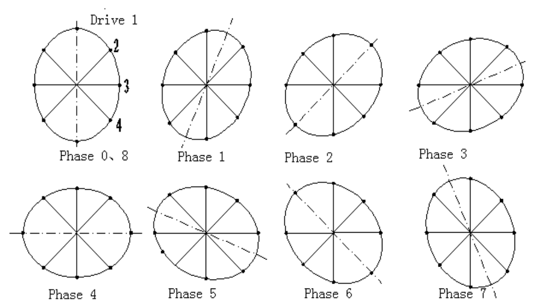

Fig.1 Structure of the Giant Magnetostrictive Harmonic Motor Fig. 2 Typical Phase Diagram of the Flex Spline

In the harmonic drive, the drive can be divided into four phases, in which the displacement pattern is identical. The reasonable match of the displacement pattern in the four-phase drive helps generate a cycle radial deformation for the flex spline (Fig. 2).

For the rest of the paper, the kinematic model and the meshing simulation of the harmonic motor are proposed in Section 2 and Section 3, respectively. Then Section 4 introduces the influence of spatial deformation cone angle on the meshing between the flex spline and the circular spline. Finally, Section 5 gives our final words.

Kinematic model of harmonic motor

In order to establish the kinematic model of GMM drive, the coordinate systems are defined as shown in Fig. 3 [2]:

$C_0(X,Y)$: fixed coordinate system at the flex spline;

$C_\gamma(X_\gamma,Y_\gamma)$: attached at the flex spline $\overline{R}$, axis Y_r is the line of symmetry of the tooth profile; the origin is located at the intersection of the characteristic curve of flexible gear and the line of symmetry of tooth profile;

$C_g(X_g,Y_g)$: the origin is at the rotation center of circular spline characteristic curve, axis Y_g is the symmetrical line of the circular spline tooth grove;

Polar coordinate system $\tilde{S}_r(\rho_r,\phi)$: the origin is at the center of the characteristic curve $\tilde{R}$ for the flex spline, the polar axis is the major axis of the deformation curve;

Polar coordinate system $\tilde{S}_g(\rho_g,\psi)$: the origin is the center of the characteristic curve for the circular spline; the polar axis coincides with the polar axis.

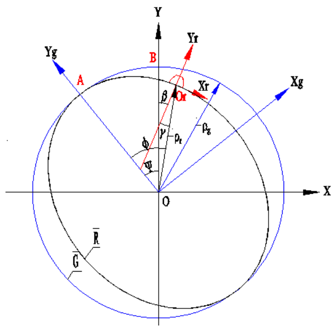

Fig.3 The Kinematic Model of the Harmonic Drive

Tab. 1 The Relative Displacement Coefficient of Each Drive

	Drive 1	Drive 2	Drive 3	Drive 4
Phase 0&8	1	0.03125	-1.025	0.03125
Phase 1	0.74625	0.74625	-0.7225	-0.7225
Phase 2	0.03125	1	0.03125	-1.025
Phase 3	-0.7225	0.74625	0.74625	-0.7225
Phase 4	-1.025	0.03125	1	0.03125
Phase 5	-0.7225	-0.7225	0.74625	0.74625
Phase 6	0.03125	-1.025	0.03125	1
Phase 7	0.74625	-0.7225	-0.7225	0.74625

The Characteristic Curve of the Flex Spline. The relative displacement coefficient is considered as ω_γ/m, where ω_γ is the radial displacement of the drive with respect to the flex spline before its deformation, m is the module. To ensure correct meshing, select the relative displacement coefficient of the flex spline deformation major axis as 1 and that of the minor axis as -1.025. The relative displacement coefficients of each drive with respect to each phase are listed in Tab. 1.

As indicated in Fig. 2 and Tab. 1, the displacement of each drive is periodic repetition because the displacement value of each driver is independent at each moment from Phase 0 to Phase 1. To obtain the displacement pattern of each drive and the deformation pattern of the corresponding flex spline, finite element method is used at each moment from Phase 0 to Phase 1. As a result, the deformation curve is shown in Fig. 4 as the calculation is performed every 4.5 degree. (Set the major axis at Phase 0 is in 90 degree).

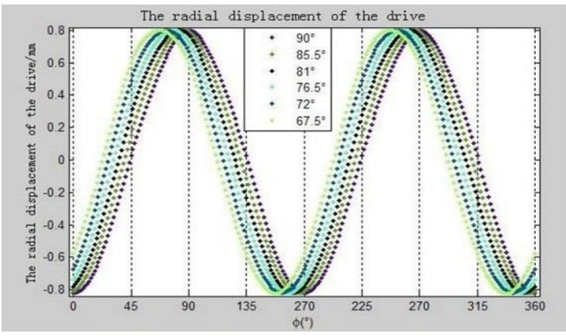

Fig. 4 The Deformation Curve of the Flex Spline

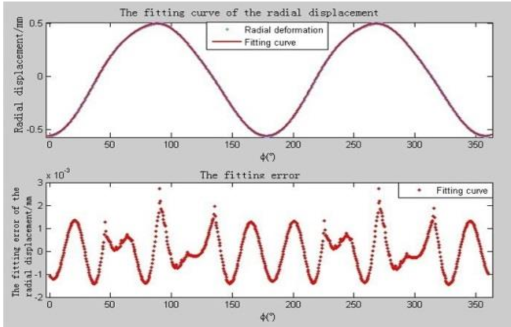

Fig. 5 Fourier Fitting Curve and its Error Analysis

As multi-point drive strategy is employed, each time the deformation curve of the flex spline is different. To minimize the error at each moment, the curve is optimized by performing Fourier fitting after averaging the number of the deformation curve at each moment.

The Fourier function in $\tilde{S}_r(\rho_r, \phi)$ is [3, 4]:

$$\rho_r(\phi) = a_0 + \sum_{i=1}^{n}[a_i * \cos(\omega * \phi) + b_i * \sin(\omega * \phi)] \tag{1}$$

where ρ_γ is the radius of the characteristic curve of the flex spline,n is a positive integer setting as 4, φ is represents the polar angle, and a_0, a_i, b_i, ω are constant. The fitting curve of the flex spline and its error curve are drawn in Fig. 5. The maximum error is 4.144×10^{-3} mm which can meet the engagement requirement.

Tooth profile Equation of the Circular Spline. Involute line tooth profile is selected as the profile of the flex spline in this paper [5]. The tooth profile equation of the flex spline in $C_\gamma(X_\gamma, Y_\gamma)$ can be described as:

$$x_r = x_r(t), y_r = y_r(t) \tag{2}$$

where t is the rotation angle when the cutter purely rolls along the pitch circle of the cut gear.

In this case, the movement pattern of a single tooth is sufficient because all the teeth share the same movement pattern. According to the envelope theory, the envelope tooth profile is the conjugate tooth profile of the selected tooth profile [6]. Based on the coordinated transformation matrix, the conjugate tooth profile in $C_g(X_g, Y_g)$ can be represented as [3, 4]:

$$\begin{cases} x_g(t,\phi) = x_r(t)\cos\beta + y_r(t)\sin\beta + \rho_r\sin(\phi-\psi) \\ y_g(t,\phi) = -x_r(t)\sin\beta + y_r(t)\cos\beta + \rho_r\cos(\phi-\psi) \\ \dfrac{\partial x_g}{\partial\phi}\bullet\dfrac{\partial y_g}{\partial t} - \dfrac{\partial y_g}{\partial\phi}\bullet\dfrac{\partial x_g}{\partial t} = 0 \\ \beta = \gamma + (\phi - \psi) \\ \gamma = \arctan\left|\rho_r^{'}/\rho_r\right| \end{cases} \tag{3}$$

Where γ is tooth deflection angle –the angle between the polar and the normal at Point O_r, β is the angle between the circular spline coordinate system and the tooth coordinate system, and ψ represents the angle between the circular spline coordinate system and the flex spline system. In addition, there are no slides between the flex spline and the circular spline, which leads to $\widehat{AB} = \widehat{AO_r}$. That means,

$$\psi = \frac{1}{r_g}\int_0^{\phi}\sqrt{\rho_r^{\,2} + \rho_r^{'2}}\,d\phi \tag{4}$$

From Equation (3) and (4), the conjugate tooth profile can be obtained [7].

Meshing Simulation of GMM Harmonic Motor

The 160 GMM motor is set as the research object and its transmission ratio is 100. The technical parameters are as follows: The teeth number of the flex spine Z_r is 200; The teeth number of the circular spline Z_g is 202; $\alpha=20°$, $m=0.8$, $x_r=3.45$, $x_g=3.53$.

Tooth Profile of the Conjugate Circular Spline. From Equation (3), the conjugate tooth profile of the circular spline is shown in Fig. 6, in which the dashed line represents the tooth profile for flex spline while the solid line is for the conjugate tooth profile.

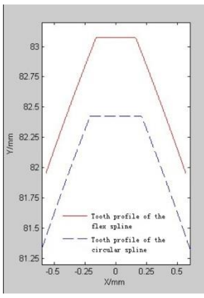

Fig. 6 Tooth Profile of Flex Spline and Circular Spline

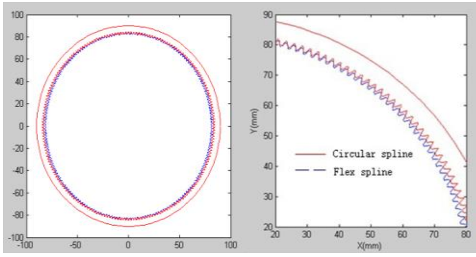

(a) Whole Map (b) Partial Map

Fig. 7 Kinematic Simulation

Kinematic Simulation. The kinematic simulation of the circular spline and the flex spline is shown in Fig. 7, in which the thick solid line is the flex spline profile and the thin solid line is the circular spline profile. As can be seen in Fig. 7(a), the circular spline fully engaged at the major axis with the flex spline before fully disengaged at the minor axis. On the other hand, the partial enlarged view Fig. 7(b) shows that there is no overlapping interference between the circular spline and the flex spline.

Tooth Trajectory of the Circular Spline. The location and trajectory of the circular spline tooth with respect to the flex spline in the whole loop that the drive moves can be obtained in Matlab with the deformation of the flex spline setting as 0.8mm. The thick (red) line in Fig. 8 is the relative trajectory of the circular spline.

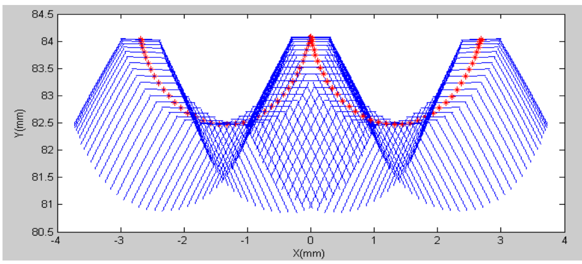

Fig. 8 Trajectory of the Circular Spline

Impact of Spatial Cone Angle on the Engagement

In order to investigate how the cone angle for different cross sections along the gear width of the flex spline deformation influences the engagement, two assumptions are proposed:

(1) The perimeter of the cross section of the neutral plane does not change but the major and minor axes vary in the process of flex spline deformation. Moreover, the shapes of various cross sections after deformation are Fourier fitting curve as before.

(2)The generatrix through major axis cross section doesn't deflect along the peripheral direction of the flex spline after the flex spline deformation, and it is always a straight line.

The Influence of the Space Deformation Cone Angle in Harmonic Drive. The deformation cone angle on the major axis δ equals 0.286° for a general flex spline with a ratio of 1 between the lenth and diameter , while that in this paper is 0.314° (Fig. 9).

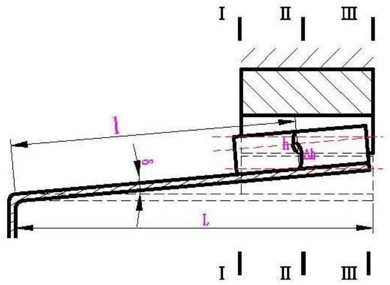

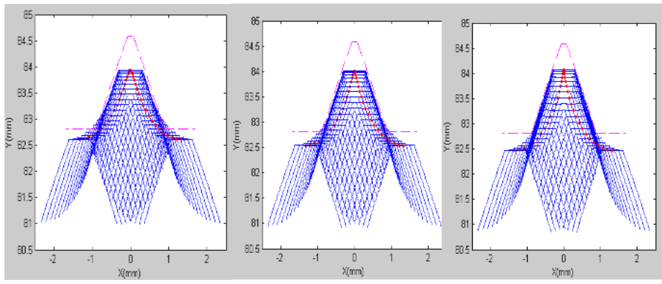

(a) Section I (b) Section II (c) Section III

Fig.9 Harmonic Drive Mesh Diagram Fig.10 Tooth Trajectory of Different Sections in Tooth Width Direction

The meshing simulation is displayed in Fig. 10. The impact of deformation cone angle on the meshing performance cannot be ignored as there are overlaps in Fig. 10(a) and Fig. 10(b).

Discussion on Equal Width Shrink. In order to achieve better meshing performance, the equal width shrinkage strategy for the circular spline is proposed. The tooth on the circular spline is changed from straight tooth to equal width shrinkage tooth so that the mesh depth for each tooth on various mesh cross section can be approximately equal (Fig. 11). As can be seen from Fig. 12, meshing overlap can be avoided and better meshing performance is achieved.

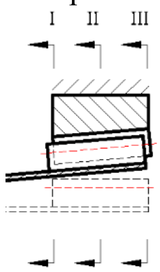

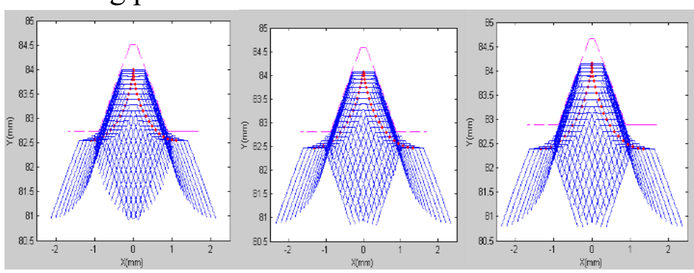

(a) Section I (b) Section II (c) Section III

Fig.11 Equal Width Shrinkage of the Circular Spline Fig. 12 Tooth trajectory of Different Cross Section

The Equal width shrinkage cone angle can be obtained by,

$$\rho_r(\phi)_I + h_{aR} = R_{aG} - B * \tan\delta \tag{5}$$

Where R_{aG} refers to the radius of the addendum circle of the circular spline , addendum coefficient h_{aG}^* is 1 and B represents the face width.

After calculation, the deformation cone angle in our example is 0.157°, and the disengaged angle is 43.0771°, thus overlap and disengagement dilemma can be avoided.

Discussion and Summary

A GMM harmonic motor with eight dots direct drive is used in this paper. The characteristic curve for the flex spline is particular which leads to some impact on the meshing performance. In order to solve this problem, Fourier transformation is used to get the mathematical description of the characteristic curve. Besides from this, a methodology based on the envelope theory to calculate the tooth profile of the circular spline when that of the flex spline is given is proposed. This helps solve the kinematic simulation as well as the parameter design. In the second part of the paper, the impact of the deformation cone angle for the flex spline on the meshing performance is discussed in details. The equal width shrinkage for the circular spline is also put forward. In addition, the calculation methodology of the shrink angle is given, by which meshing overlap and disengagement in minor axis are eliminated.

Although detailed method for tooth profile calculation and improvement measures are given in this paper, these discussion are mainly from theoretical simulation. In the future, more work need to be done in tooth profile optimization.

Acknowledgements

This work is supported by National Natural Science Foundation of China (approval No. 51275069).

References

[1] ZHU L. J., GAO W. Q., ZHAO X, et al., Research on harmonic gear based on giant magnetostrictive material (in Chinese) , Magnetic Materials and Devices. 2009, 40 (3).

[2] FAN Y. G., CAO B. H., Harmonic gear drive technical manual (in Chinese) Beijing: National Defense Industry Press, 1995.

[3] Mathews J. H., Fink K. D., Numerical methods (MATLAB), fourth version (in Chinese), ZHOU L., Chen Y., QIAN F., Translation. Beijing: Electronic Industry Press, 2005:230-237.

[4] DONG H. M.， ZHANG C. M., Study on deformation function of flexible gear under load and its tooth profile modification of tooth-locked-output harmonic drive (in Chinese), Mechanical Transmission, 2011， 35 (7).

[5] SHEN Y. W., YE Q. T., Harmonic gear theory and design, Beijing: Machinery Industry the Press, 1985:239 -241.

[6] XIE J. R., Meshing analysis method of harmonic drive using ellipse gam generator (in Chinese), Optical Machinery, 1980, 3: 33239.

[7] ZHANG Y. Meshing theory and analysis of harmonic transmission with 1/4 short flexspline for humanoid robot (in Chinese), Harbin Institute of Technology, 2011(6): 16-19.

Applied Mechanics and Materials
ISSN: 1662-7482, Vol. 421, pp 16-22
doi:10.4028/www.scientific.net/AMM.421.16

Online: 2013-09-11

Passivity-based Stabilization of Underactuated Mechanical Systems

Shanshan Wu[a], Wei Huo[b]

The Seventh Research Division, Science and Technology on Aircraft Control Laboratory Beihang University, Beijing 100191, P.R.China

[a]email: viv533@163.com, [b]email: weihuo@buaa.edu.cn

Keywords: Underactuated systems; Stabilization; Controller design; Passivity; Pendubot.

Abstract. A new stabilization control method for underactuated linear mechanical systems is presented in this paper. By proper setting the desired closed-loop system, the matching condition for controller design is reduced to one equation and an adjustable parameter (damping coefficient) is introduced to the controller. Stability of the closed-loop system is proved based on passivity. As an application example, stabilization control of 2-DOF Pendubot is studied. The system is linearized at its equilibrium point and the proposed controller design method is applied to the linearized system. The procedure of solving matching condition and design controller for the Pendubot is provided. The simulation results verify feasibility of the proposed method.

Introduction

The underactuation of a mechanical system means that the dimension of its control vector is less than that of its configuration vector. In practical engineering, many mechanical systems are underactuated systems since underactuated mechanical systems can reduce cost and weight of the systems. Moreover, the idea of underactuation can be utilized to control systems with failed components. Therefore, the more and more attention has been devoted to controller design for underactuated mechanical systems in recent years.

At present, two effective methods to design controller for underactuated mechanical system are *Controlled Lagrangians(CL)* and *Interconnection & Damping Assignment Passivity-based Control(IDA-PBC)* . The *CL* method for underactuated mechanical systems whose actuated variables are symmetry group variables was introduced in[1,2]. The *CL* method for general mechanical systems with unactuation degree one was developed in [3,4,5]. The control of mechanical system was studied with Hamiltonian and *IDA-PBC* method was introduced in [6,7,8].The equivalence of *CL* and *IDA-PBC* methods was discussed in [9].

Motivated by *CL* and *IDA-PBC* methods, a simple stabilization method for underactuated linear mechanical systems is presented in this paper. By proper setting the damping matrix in desired closed-loop system, the matching condition for controller is reduced to only one equation, which greatly facilitates control design for underactuated systems. The 2-DOF Pendubot is used as an application example to show the controller design procedure. The simulation results verify effectiveness of the presented method.

Preliminary

Consider following nonlinear system:

$$\dot{x} = f(x) + g(x)u, \quad y = h(x) \ , \tag{1}$$

where $x \in \boldsymbol{R}^n$, $u \in \boldsymbol{R}^m$, $y \in \boldsymbol{R}^m$; f is local Lipschitz, g and h are continuous, $f(0) = h(0) = 0$.

Definition 1[10]**:** System Eq. 1 is passive if there exists a positive semi-definite continuous differentiable function $S(x)$ (called storage function) such that

$$u^T y \geq \dot{S}, \quad \forall (x,u) \in \boldsymbol{R}^n \times \boldsymbol{R}^m .$$

Theorem 1[10]**:** If system Eq. 1 is passive, it can be stabilized asymptotically by negative feedback control with constant gain $u=-Ky\ (K>0)$, if and only if system Eq. 1 is zero state detectable.

Controller Design

System Dynamics. Consider following underactuated linear mechanical system:

$$M\ddot{q}+Kq=u=Ov\,, \tag{2}$$

where $q\in \boldsymbol{R}^n$ and $\dot{q}\in \boldsymbol{R}^n$ are generalized coordinates and velocities of the system, respectively; $M=M^T>0$ and K are $n\times n$ constant matrices; $u\in \boldsymbol{R}^n$ and $v\in \boldsymbol{R}^m$ are inputs and $n\times m$ constant matrix O is input coupling matrix satisfying $\mathrm{rank}(O)=m<n$. Note that an admissible input u should satisfy $\bar{O}u=0$, where $\bar{O}O=0$.

Desired Closed-loop System and Its Stability Analysis. Design desired closed-loop system in following form:

$$\bar{M}\ddot{q}+\bar{D}\dot{q}+\bar{K}q=0\,, \tag{3}$$

where $\bar{M}=\bar{M}^T>0$ and $\bar{K}=\bar{K}^T>0$ are $n\times n$ constant positive definite matrices, $\bar{D}=\bar{M}M^{-1}OK_vO^TM^{-1}\bar{M}$ and $K_v={K_v}^T>0$ is a $m\times m$ constant positive definite damping coefficient matrix. The desired closed-loop system Eq. 4 can be written as following system:

$$\bar{M}\ddot{q}+\bar{K}q=\bar{M}M^{-1}Ou_d,\quad y=O^TM^{-1}\bar{M}\dot{q},\quad u_d=-K_vy\ (K_v>0)\,. \tag{4}$$

We can prove that the open-loop system of system Eq. 4 (i.e. the system composed by the first and second equations of Eq. 4) is passive for input u_d and output y. The first equation of Eq. 4 gives

$$\ddot{q}=-\bar{M}^{-1}\bar{K}q+M^{-1}Ou_d\,. \tag{5}$$

Choose positive definite function $\bar{E}(q,\dot{q})=\dot{q}^T\bar{M}\dot{q}/2+q^T\bar{K}q/2$ as the storage function, using Eq. 5 and the second equation of Eq. 4 we have

$$\dot{\bar{E}}=\ddot{q}^T\bar{M}\dot{q}+\dot{q}^T\bar{K}q={u_d}^TO^TM^{-1}\bar{M}\dot{q}={u_d}^Ty\,.$$

From Definition 1, we know that the open-loop system of system Eq. 4 is passive.

Furthermore, we can prove that the open-loop system of system Eq. 4 is zero state observable. Define $x=[q^T,\dot{q}^T]^T$, the open-loop system of system Eq. 4 can be rewritten as:

$$\dot{x}=\begin{bmatrix}0 & I\\ -\bar{M}^{-1}\bar{K} & 0\end{bmatrix}x+\begin{bmatrix}0\\ M^{-1}O\end{bmatrix}u_d\triangleq Ax+Bu_d,\quad y=\begin{bmatrix}0 & O^TM^{-1}\bar{M}\end{bmatrix}x\triangleq Cx$$

Its observabile matrix

$$W_c\triangleq\begin{bmatrix}C\\ CA\\ \vdots\\ CA^{n-1}\end{bmatrix}=\begin{bmatrix}0 & O^TM^{-1}\bar{M}\\ -O^TM^{-1}\bar{M}Q & 0\\ 0 & -O^TM^{-1}\bar{M}Q\\ O^TM^{-1}\bar{M}Q^2 & 0\\ \vdots & \vdots\\ 0 & (-1)^{n-1}O^TM^{-1}\bar{M}Q^{n-1}\\ (-1)^nO^TM^{-1}\bar{M}Q^n & 0\end{bmatrix}, \tag{6}$$

where $Q=\bar{M}^{-1}\bar{K}$. Since

$$\operatorname{rank}\begin{bmatrix} -O^T M^{-1}\bar{M}Q \\ O^T M^{-1}\bar{M}Q^2 \\ \vdots \\ (-1)^n O^T M^{-1}\bar{M}Q^n \end{bmatrix} = \operatorname{rank}\begin{bmatrix} O^T M^{-1}\bar{M} \\ -O^T M^{-1}\bar{M}Q \\ \vdots \\ (-1)^{n-1} O^T M^{-1}\bar{M}Q^{n-1} \end{bmatrix} = \operatorname{rank}\begin{bmatrix} O^T \\ O^T M^{-1}\bar{M}Q\bar{M}^{-1}M \\ \vdots \\ O^T M^{-1}\bar{M}Q^{n-1}\bar{M}^{-1}M \end{bmatrix}$$
$$= \operatorname{rank}\begin{bmatrix} O^T & 0 & \cdots & 0 \\ 0 & \ddots & & \vdots \\ \vdots & & \ddots & 0 \\ 0 & \cdots & 0 & O^T \end{bmatrix}\begin{bmatrix} I \\ M^{-1}\bar{M}Q\bar{M}^{-1}M \\ \vdots \\ M^{-1}\bar{M}Q^{n-1}\bar{M}^{-1}M \end{bmatrix} = n \tag{7}$$

From Eq. 6 and Eq. 7, we know $\operatorname{rank} W_c = 2n$, which implies that the open-loop system of system Eq. 4 is zero state observable.

Since the open-loop system of system Eq. 4 is passive and zero state observable, from Theorem 1 we conclude that the closed-loop system Eq. 4 is asymptotically stable under the feedback control $u_d = -K_v y\ (K_v > 0)$. It means that the desired system Eq. 3 is asymptotically stable.

Determining Matching Condition and Controller. Premultiplying Eq. 3 by $M\bar{M}^{-1}$ gives

$$M\ddot{q} + M\bar{M}^{-1}\bar{D}\dot{q} + M\bar{M}^{-1}\bar{K}q = 0\,. \tag{8}$$

Equating the accelerations terms in Eq. 2 and Eq. 8 yields

$$\begin{aligned} u = Ov &= (K - M\bar{M}^{-1}\bar{K})q - M\bar{M}^{-1}\bar{D}\dot{q} \\ &= (K - M\bar{M}^{-1}\bar{K})q - OK_v O^T M^{-1}\bar{M}\dot{q}\,. \end{aligned} \tag{9}$$

If u is an admissible control input, it must satisfy following condition:

$$\bar{O}u = \bar{O}(K - M\bar{M}^{-1}\bar{K})q = 0\,. \tag{10}$$

Since Eq. 10 hold for arbitrary generalized coordinates q, we obtain the matching condition for control as follows:

$$\bar{O}(K - M\bar{M}^{-1}\bar{K}) = 0\,. \tag{11}$$

If $\bar{M}^{-1}$ and $\bar{K}$ can be solved from the matching condition Eq. 11, premultiplying Eq. 9 by $\hat{O} \triangleq (O^T O)^{-1} O^T$ gives the admissible control law

$$v = \hat{O}(K - M\bar{M}^{-1}\bar{K})q - K_v O^T M^{-1}\bar{M}\dot{q}\,. \tag{12}$$

Applying Passivity-Based Control Design to 2-DOF Pendubot

2-DOF Pendubot is a two-link underactuated planar robot as illustrated in Fig. 1. Its first joint is actuated, but the second one is unactuated. The dynamical equation of Pendubot is as follows[11]:

$$\begin{bmatrix} \frac{1}{3}m_1 l_1^2 + m_2 l_1^2 + \frac{1}{3}m_2 l_2^2 + m_2 l_1 l_2 c_2 & \frac{1}{3}m_2 l_2^2 + \frac{1}{2}m_2 l_1 l_2 c_2 \\ \frac{1}{3}m_2 l_2^2 + \frac{1}{2}m_2 l_1 l_2 c_2 & \frac{1}{3}m_2 l_2^2 \end{bmatrix}\ddot{\theta}$$
$$-\frac{1}{2}m_2 l_1 l_2 s_2 \begin{bmatrix} 2\dot{\theta}_1\dot{\theta}_2 + (\dot{\theta}_2)^2 \\ -(\dot{\theta}_1)^2 \end{bmatrix} - g\begin{bmatrix} (m_2 l_1 + \frac{1}{2}m_1 l_1)s + \frac{1}{2}m_2 l_2 s_{1+2} \\ \frac{1}{2}m_2 l_2 s_{1+2} \end{bmatrix} = \begin{bmatrix} u_1 \\ 0 \end{bmatrix}, \tag{13}$$

where m_1 and m_2 are the mass of link 1 and link 2, l_1 and l_2 are the lengths of link 1 and link 2, θ_1 and θ_2 are the angles of link 1 and link 2, respectively.

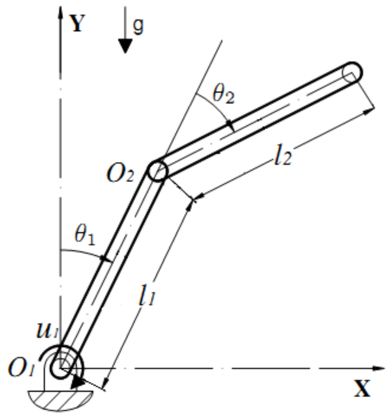

Figure 1. 2-DOF Pendubat

Since the origin $(\theta_1,\theta_2,\dot{\theta}_1,\dot{\theta}_2)=(0,0,0,0)$ is an equilibrium point of the system Eq. 13, it can be linearized about the origin to following linear system in the form as Eq. 2, where $q=[\theta_1 \quad \theta_2]^T$, $O=[1 \quad 0]^T$, $v=u_1$,

$$M=\begin{bmatrix} \frac{1}{3}m_1l_1^2+m_2l_1^2+\frac{1}{3}m_2l_2^2+m_2l_1l_2 & \frac{1}{3}m_2l_2^2+\frac{1}{2}m_2l_1l_2 \\ \frac{1}{3}m_2l_2^2+\frac{1}{2}m_2l_1l_2 & \frac{1}{3}m_2l_2^2 \end{bmatrix} \triangleq \begin{bmatrix} m_{1o} & m_{2o} \\ m_{2o} & m_{3o} \end{bmatrix},$$

$$K=-g\begin{bmatrix} m_2l_1+\frac{1}{2}m_1l_1+\frac{1}{2}m_2l_2 & \frac{1}{2}m_2l_2 \\ \frac{1}{2}m_2l_2 & \frac{1}{2}m_2l_2 \end{bmatrix} \triangleq \begin{bmatrix} k_{1o} & k_{2o} \\ k_{2o} & k_{3o} \end{bmatrix}.$$

Let $\bar{O}\triangleq[0 \quad 1]$ such that $\bar{O}O=0$. Define $\bar{M}^{-1}=\begin{bmatrix} m_{1c} & m_{2c} \\ m_{2c} & m_{3c} \end{bmatrix}$, $\bar{K}=\begin{bmatrix} k_{1c} & k_{2c} \\ k_{2c} & k_{3c} \end{bmatrix}$, from $\bar{M}>0$ we know $m_{1c}>0$ and $m_{1c}m_{3c}-m_{2c}{}^2>0$. The matching conditions Eq. 11 can be written as

$$[k_{2o} \quad k_{3o}]=[m_{2o}m_{1c}+m_{3o}m_{2c} \quad m_{2o}m_{2c}+m_{3o}m_{3c}]\begin{bmatrix} k_{1c} & k_{2c} \\ k_{2c} & k_{3c} \end{bmatrix}. \tag{14}$$

If $m_{2o}m_{2c}+m_{3o}m_{3c}\neq 0$, from Eq. 14 we get

$$k_{2c}=\eta k_{1c}+\frac{k_{2o}}{m_{2o}m_{2c}+m_{3o}m_{3c}}, \quad k_{3c}=\eta^2k_{1c}+\frac{\eta k_{2o}+k_{3o}}{m_{2o}m_{2c}+m_{3o}m_{3c}}, \tag{15}$$

where $\eta=-\frac{m_{2o}m_{1c}+m_{3o}m_{2c}}{m_{2o}m_{2c}+m_{3o}m_{3c}}$. So $|\bar{K}|=\frac{(k_{2o}m_{3o}+k_{3o}m_{2o})m_{2c}k_{1c}+(k_{3o}m_{3o}m_{3c}+k_{2o}m_{2o}m_{1c})k_{1c}-k_{2o}{}^2}{(m_{2o}m_{2c}+m_{3o}m_{3c})^2}$.

Choosing $k_{1c}>0$ and $m_{2c}<-\frac{k_{3o}m_{3o}m_{3c}+k_{2o}m_{2o}m_{1c}}{k_{2o}m_{3o}+k_{3o}m_{2o}}+\frac{k_{2o}{}^2}{(k_{2o}m_{3o}+k_{3o}m_{2o})k_{1c}}$ can guarantee $\bar{K}>0$.

Therefore, the elements of $\bar{M}^{-1}$ should satisfy:

$$m_{1c} > 0, m_{1c}m_{3c} - m_{2c}{}^2 > 0, m_{1o}m_{2c} + m_{2o}m_{3c} \neq 0, m_{2c} < -\frac{k_{3o}m_{3o}m_{3c} + k_{2o}m_{2o}m_{1c}}{k_{2o}m_{3o} + k_{3o}m_{2o}} + \frac{k_{2o}{}^2}{(k_{2o}m_{3o} + k_{3o}m_{2o})k_{1c}}.$$

We can prove that these conditions can hold simultaneously. In fact, for any $m_{1c} > 0$, choose

$$m_{3c} = k_{2o}m_{2o}m_{1c}/(k_{3o}m_{3o}) \tag{16}$$

Since $m_{2o} > 0$, $m_{3o} > 0$, $k_{2o} < 0$, $k_{3o} < 0$, we know $k_{3o}m_{3o}m_{3c} + k_{2o}m_{2o}m_{1c} = -2\sqrt{k_{2o}m_{2o}k_{3o}m_{3o}}\sqrt{m_{1c}m_{3c}}$. It is easy to verify by calculation that $k_{2o}m_{3o} \neq k_{3o}m_{2o}$, so $k_{2o}m_{3o} + k_{3o}m_{2o} < -2\sqrt{k_{3o}m_{2o}k_{2o}m_{3o}} < 0$ and $\frac{k_{3o}m_{3o}m_{3c} + k_{2o}m_{2o}m_{1c}}{k_{2o}m_{3o} + k_{3o}m_{2o}} < \frac{2\sqrt{k_{3o}m_{3o}k_{2o}m_{2o}}\sqrt{m_{1c}m_{3c}}}{2\sqrt{k_{2o}m_{2o}k_{3o}m_{3o}}} = \sqrt{m_{1c}m_{3c}}$, which means that choosing k_{1c} large enough can guarantee

$$-\sqrt{m_{1c}m_{3c}} < -\frac{k_{3o}m_{3o}m_{3c} + k_{2o}m_{2o}m_{1c}}{k_{2o}m_{3o} + k_{3o}m_{2o}} + \frac{k_{2o}{}^2}{(k_{2o}m_{3o} + k_{3o}m_{2o})k_{1c}}. \tag{17}$$

So we can choose m_{2c} satisfying

$$-\sqrt{m_{1c}m_{3c}} < m_{2c} < -\frac{k_{3o}m_{3o}m_{3c} + k_{2o}m_{2o}m_{1c}}{k_{2o}m_{3o} + k_{3o}m_{2o}} + \frac{k_{2o}{}^2}{(k_{2o}m_{3o} + k_{3o}m_{2o})k_{1c}}. \tag{18}$$

We can verify $-\frac{2k_{2o}m_{2o}}{k_{2o}m_{3o} + k_{3o}m_{2o}} + \frac{k_{2o}}{k_{3o}} = \frac{m_{3o} - m_{2o}}{m_{3o} + m_{2o}} < 0$ and $m_{2c} + \frac{m_{3o}m_{3c}}{m_{2o}} < -\frac{k_{3o}m_{3o}m_{3c} + k_{2o}m_{2o}m_{1c}}{k_{2o}m_{3o} + k_{3o}m_{2o}} + \frac{k_{2o}{}^2}{(k_{2o}m_{3o} + k_{3o}m_{2o})k_{1c}} + \frac{m_{3o}m_{3c}}{m_{2o}} = (-\frac{2k_{2o}m_{2o}}{k_{2o}m_{3o} + k_{3o}m_{2o}} + \frac{k_{2o}}{k_{3o}})m_{1c} + \frac{k_{2o}{}^2}{(k_{2o}m_{3o} + k_{3o}m_{2o})k_{1c}} < 0$, it implies $m_{2o}m_{2c} + m_{3o}m_{3c} \neq 0$.

After $\bar{M}^{-1}$ and $\bar{K}$ are obtained, we get the matching control law from Eq. 12:

$$\begin{aligned} v = {} & [k_{1o} - (m_{1o}m_{1c} + m_{2o}m_{2c})k_{1c} - (m_{1o}m_{2c} + m_{2o}m_{3c})k_{2c}]\theta_1 \\ & + [k_{2o} - (m_{1o}m_{1c} + m_{2o}m_{2c})k_{2c} - (m_{1o}m_{2c} + m_{2o}m_{3c})k_{3c}]\theta_2 \\ & - \frac{k_v}{(m_{1o}m_{3o} - m_{2o}{}^2)(m_{1c}m_{3c} - m_{2c}{}^2)}\left[(m_{2o}m_{2c} + m_{3o}m_{3c})\dot{\theta}_1 - (m_{2o}m_{1c} + m_{3o}m_{2c})\dot{\theta}_2\right] \end{aligned} \tag{19}$$

where $k_v > 0$ is an adjustable damping gain.

Above controller design procedure for 2-DOF Pendubot can be summarized as follows:

1) Choose $m_{1c} > 0$ and determine m_{3c} by Eq. 16;

2) Choose $k_{1c} > 0$ satisfies Eq. 17;

3) Determine m_{2c} by Eq. 18;

4) Determine k_{2c} and k_{3c} by Eq. 15;

5) Determine $\bar{D} = \bar{M}M^{-1}OK_vO^TM^{-1}\bar{M}$, where $K_v = K_v{}^T > 0$;

6) Determine control v by Eq. 19.

Simulation

For 2-DOF Pendubot, let $m_1 = 0.6$ [kg], $l_1 = 0.6$ [m], $m_2 = 0.4$ [kg], $l_2 = 0.4$ [m] [11]. Follow the proposed control design procedure, determine m_{1c}=100, m_{2c}=−170, $m_{3c} = 325$, k_{1c}=1, $k_{2c} = 0.8462$, $k_{3c} = 0.7413$. Choose $k_v = 1$ and from Eq. 19 determine control:

$$v{=}2.3354\theta_1 + 6.2725\theta_2 + 0.5851\dot{\theta}_1 + 0.3987\dot{\theta}_2$$

The simulation results for initial state $(\theta_1, \theta_2, \dot{\theta}_1, \dot{\theta}_2) = (0.1[\text{rad}], -0.1[\text{rad}], 0[\text{rad/s}], 0[\text{rad/s}])$ are illustrated in Fig. 2.

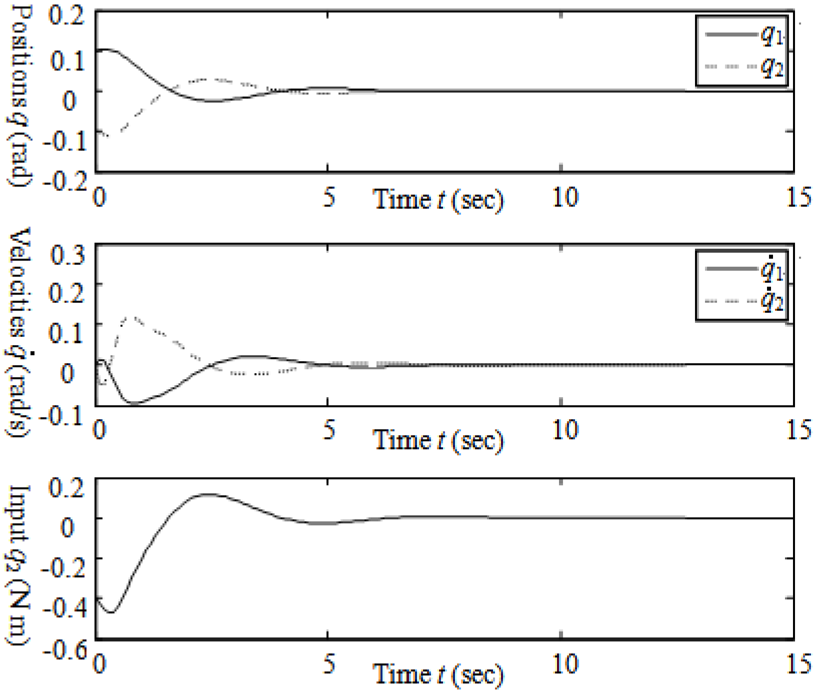

Figure 2. Simulation results of controlled 2-DOF Pendubot

Conclusion

A novel stabilization control design method for underactuated linear mechanical systems is developed in this paper. Based on passivity control theory a proper desired closed-loop system is designed such that the matching condition for ad controller is simplified, which facilitates solving the matching condition and controller design. The proposed method is applied to 2-DOF Pendubot to demonstrate the detailed procedure of controller design. The simulation results are provided to verify the feasibility of the proposed design method.

Acknowledgement

This work was supported by the National Natural Science Foundation of China under Grant No.61074010.

References

[1] A.M. Bloch, N.E. Leonard and J.E. Marsden: Stabilization of mechanical systems using controlled Lagrangians. *Proc. of the 36th IEEE Conference on Decision and Control*, p2356. (1997).

[2] A.M. Bloch, D.E. Chang, N.E. Leonard: Controlled Lagrangians and the stabilization of mechanical systems II: Potential shaping. IEEE Trans. Autom. Control, Vol. 46 (2001) , p. 1556.

[3] D. Auckly, L. Kapitanski and W. White: Control of nonlinear underactuated systems. Communications on Pure and Applied Mathematics, Vol. 53 (2000) , p. 354.

[4] D. Auckly and L. Kapitanski: On the λ-equations for matching control laws. SIAM Journal on Control and Optimization, Vol. 41 (2001) , p. 1372.

[5] J. Hamberg: General matching conditions in the theory of controlled Lagrangians. *Proceedings of the 38th Conference on Decision and Control*, p. 2519. (1999)

[6] R. Ortega, A.J. van der Schaft and B.Maschke: Interconnection and damping assignment passivity-based control of port-controlled Hamiltonian systems. Automatica, Vol. 38 (2002) , p.585.

[7] R. Ortega, M.W. Spong and F. Gomez-Estern: Stabilization of underactuated mechanical systems via interconnection and damping assignment. IEEE Trans. Autom. Control, Vol. 47(2003) , p.1218.

[8] J.A. Acosta, R. Ortega and A. Astolfi: Interconnection and damping assignment passivity-based control of mechanical systems with underactuation degree one. IEEE Trans. Autom. Control, Vol. 50(2005) , p. 1936.

[9] G. Blankenstein, R. Ortega, M.W. Spong: The matching conditions of controlled Lagrangians and IDA-passivity based control. International Journal of Control, Vol. 75(2002) , p. 645.

[10] C. B. Feng: *The Robust Control of nonlinear system* (Science Press, Beijing 2004).

[11] M.Q. Li: Controlled Lagrangians Method and Its Applications to Control of Underactuated Systems (Ph. D., Beihang University, China 2009).

Applied Mechanics and Materials
ISSN: 1662-7482, Vol. 421, pp 23-28
doi:10.4028/www.scientific.net/AMM.421.23

Online: 2013-09-11

The Material Nonlinear Analysis of Bioprosthetic Heart Valve on Suture Densities

Xia Zhang[1.a], Quan Yuan[1.b*] , Jun Zhang[2.c] , Xu Huang[1.d] , Hua Cong[3.e]

[1]School of Mechanical Engineering, Shandong University, Key Laboratory of High-efficiency and Clean Mechanical Manufacture, Shandong University Ministry of Education,Jinan 250061, P. R. China;

[2]School of Physical Education,Shandong University,Jinan 250061, P. R. China.

[3]School of Medicine ,Shandong University,Jinan 250061, P. R. China.

[a]409041529@qq.com ; [b]yuanquan66@sdu.edu.cn.

[*]Corresponding author

Keywords: Finite element method; Bioprosthetic heart valve; Stress distribution; Suture density.

Abstract. In order to investigate the effect of suture density on the dynamic behavior of bioprosthetic heart valve with nonlinear material and improve long term durability of bioprosthetic heart valve, we establish the ellipsoidal leaflets and paraboloidal leaflets models via computer aided design. Based on the parametric models of the heart valve, four kinds of suture density（100,70,50 and 35 suture points on the attachment edge of the bioprosthetic heart valve）are analyzed by using finite element method. The finite element analysis results are compared with each valve model. It shows that suture density has a significant effect on the dynamic behavior of the bioprosthetic heart valve, which lead to different stress peak values, different stress distributions and deformation. The finite element analysis of the BHV could provide direct and useful information for the BHV designer.

Introduction

Bioprosthetic heart valve has been widely used since1965. During the 1980s the scale of the bioprosthetic heart valve has been closed to the mechanical heart valve[1]. Bioprosthetic heart valve consists of valvular leaflets, supporting stent and sutural ring. The flow field of bioprosthetic heart valve is similar to that of the human heart valve. Valvular leaflets made with polymer materials of porcine or bovine pericardial can be opened or closed by ejected blood. The supporting stent acts not only as a configuration functional part but also as a component to support and bear forces. The flow field of BHV is similar to that of the human heart valve. Its flow pattern is central-like. Although its function is improved in antihenolysis and antithrombotic, the efficiency in device design of the BHV is still not satisfied [2]. In order to improve long-term durability of BHV, stress distribution of BHVs are analyzed and compared based on finite element method. We create the paraboloidal and the ellipsoidal leaflets for nonlinear dynamic analysis [3]. This work could provide useful information for the bioprosthetic heart valve designer.

Method

Model of the BHV. The bioprosthetic heart valve is often made with porcine or bovine pericardial which belong to the hyperelastic material [4,5]. The properties of hyperelastic material is similar to rubber. The mechanical properties can be obtained from the uniaxial tensile experiments. The data of the experiment is shown in table 1.

Table1. Orthogonal anisotropic parameters

Property	PET
Circumferential stress(Mpa)	4600
Radial stress(Mpa)	4600
Thickness direction stress(Mpa)	60000
xy direction shear stress(Mpa)	15862
yz direction of shear stress(Mpa)	4252
xz direction of shear stress(Mpa)	4252
*xy*direction poisson's ratio	0.45
*yz*direction poisson's ratio	0.0345
*xz*direction poisson's ratio	0.0345
Thickness(mm)	0.5
Density	1.01 e^{-9}

Finite Division . We use import the model of the ellipsoidal heart valve into the ANSYS software and the ANSYS software’s subprogram-SHELL163 is used to analyze the stress distribution. We assume that the thickness of the valve leaflets is 0.5mm. The solid model of the valve leaflets is divided into grid by subprogram of ANSYS software as shown in Fig.1

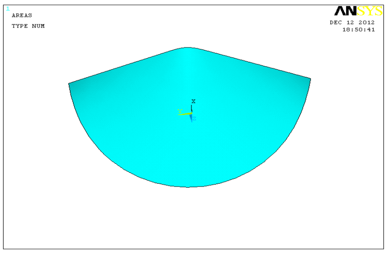

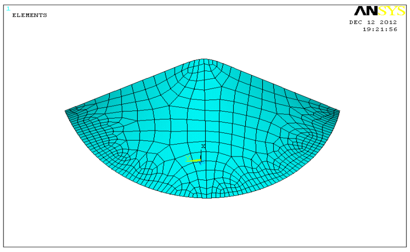

Figure 1(a). IGES file of valve leaflet Figure 1(b). Mesh division of valve leaflet

Boundary Condition of BHV. For rigid stent material, displacement vectors of every point in brim of a leaf is zero, so the boundry condition can be expressed as:

$$\{\delta\} = \{ u , v , w , Qx , Qy , Qz \}^{T} = \{0, 0, 0 , 0 , 0, 0\}^{T}$$

Pressure Loading Pattern. To represent loading during the bioprosthetic heart valve closing, the following pressure-time relationship is assumed in this work. The pressure on the bioprosthetic heart valve is modeled as to ramp, indicating an increase of pressure from 0 to 0.016Mpa[6].

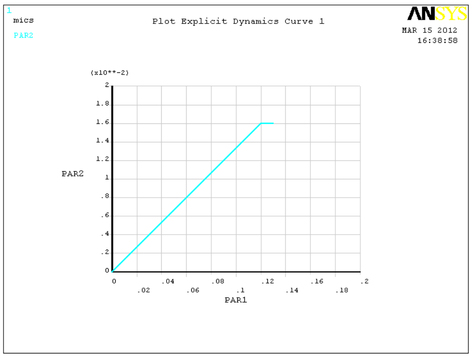

Figure 2. Pressure loading curve for BHV

Result and Discussion

The finite element results of the ellipsoidal and paraboloidal heart valves are presented in Fig3,4,5and 6. We focus our attention on the peak stress and stress distribution of the valve leaflets.

Stress Distribution of Ellipsoidal Heart Valve.

Suture points:0.001s 0.003s 0.005s 0.007s 0.009s 0.011s

35

50

70

100

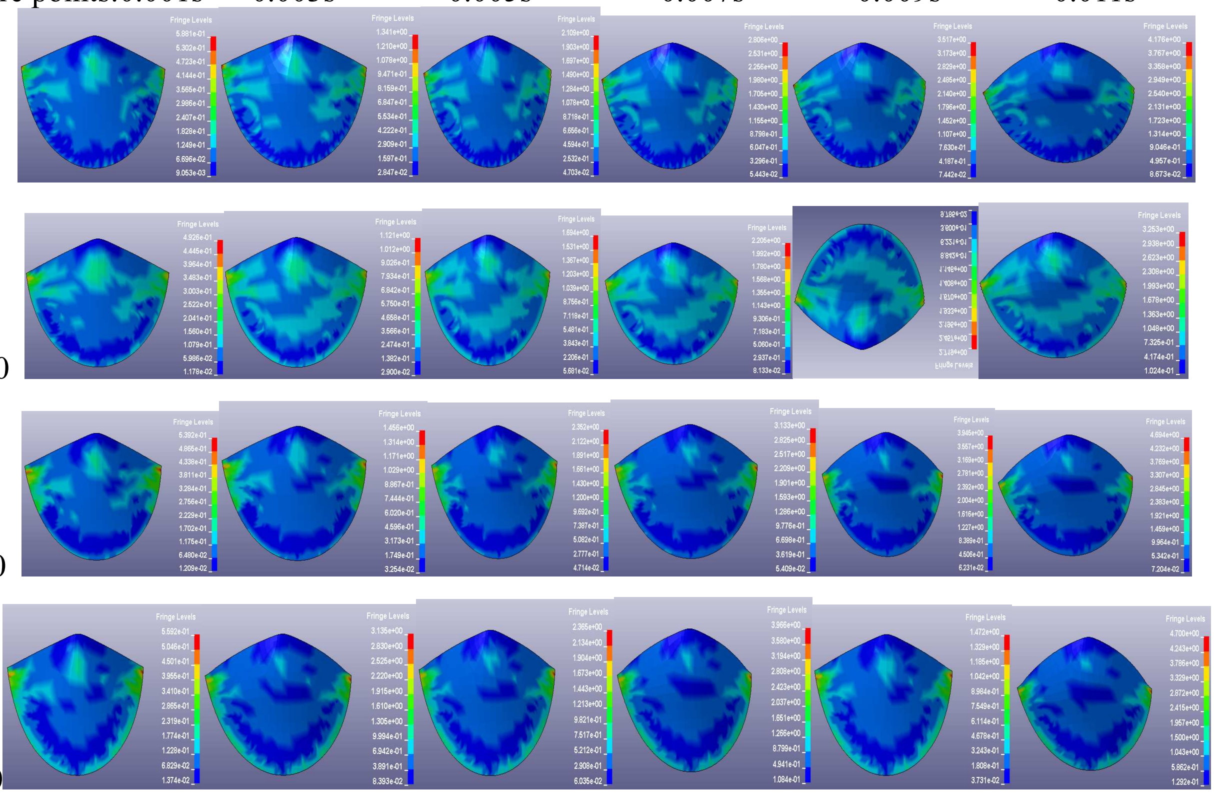

Figure 3. Stress distribution of ellipsoidal valve leaflets with different suture density

According to the finite element analysis results, we can conclude that during the loading process, the deformation of valve leaflets is larger, non-uniform stress appears the abdomen and edge of valve leaflets, This kind of phenomenon is more obvious at the attachment edge of valve leaflets with 35and50 suture points.Although the stress distribution is not uniform, at the beginning of the loading process, the stress concentration appears at the top of the attachment edge, As the loading process, the stress concentration area gradually decreases, and the last time the stress concentration phenomenon disappeared basically.

Suture points: 35 50

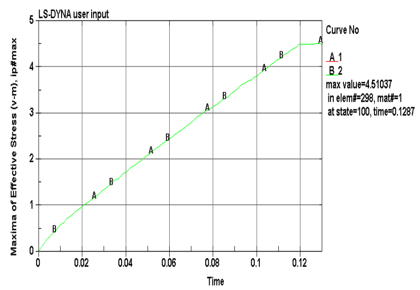

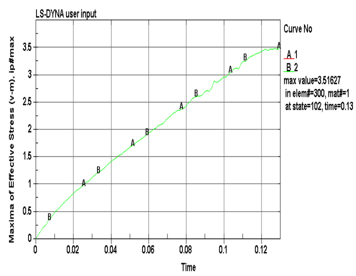

70 100

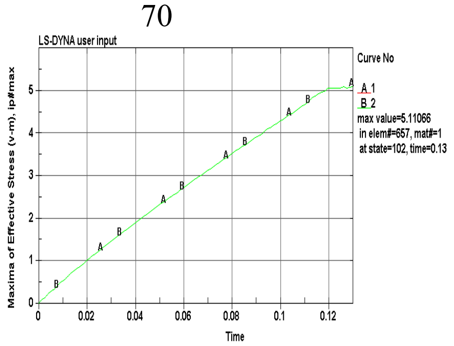

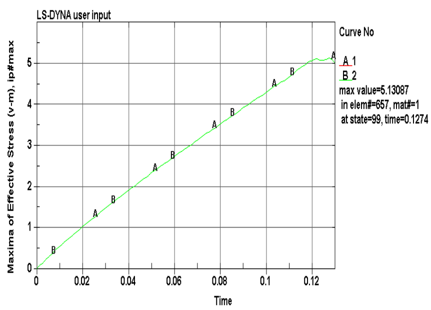

Figure 4. Stress distribution of ellipsoidal valve leaflet

It can be seen from the figure 4 that the maximum stress of valve leaflet within 0 s to 0.12 s approximate linear growth, maximum stress within 0.12 s to 0.13 s remains the same. And the maximum peak occur within 0.12 s to 0.13 s. The maximum stress with 35, 50 ,70 and100 suture points is 4.51Mpa, 3.51Mpa, 5.11Mpa and 5.13Mpa. The maximum stress with 50suture points is much smaller than that with 35,70 and 100 suture points. We can conclude that the 50 suture points has good dynamic mechanics performance.

Stress Distribution of paraboloidal Heart Valve

Suture points: 0.001s 0.003s 0.005s 0.007s 0.009s 0.011s

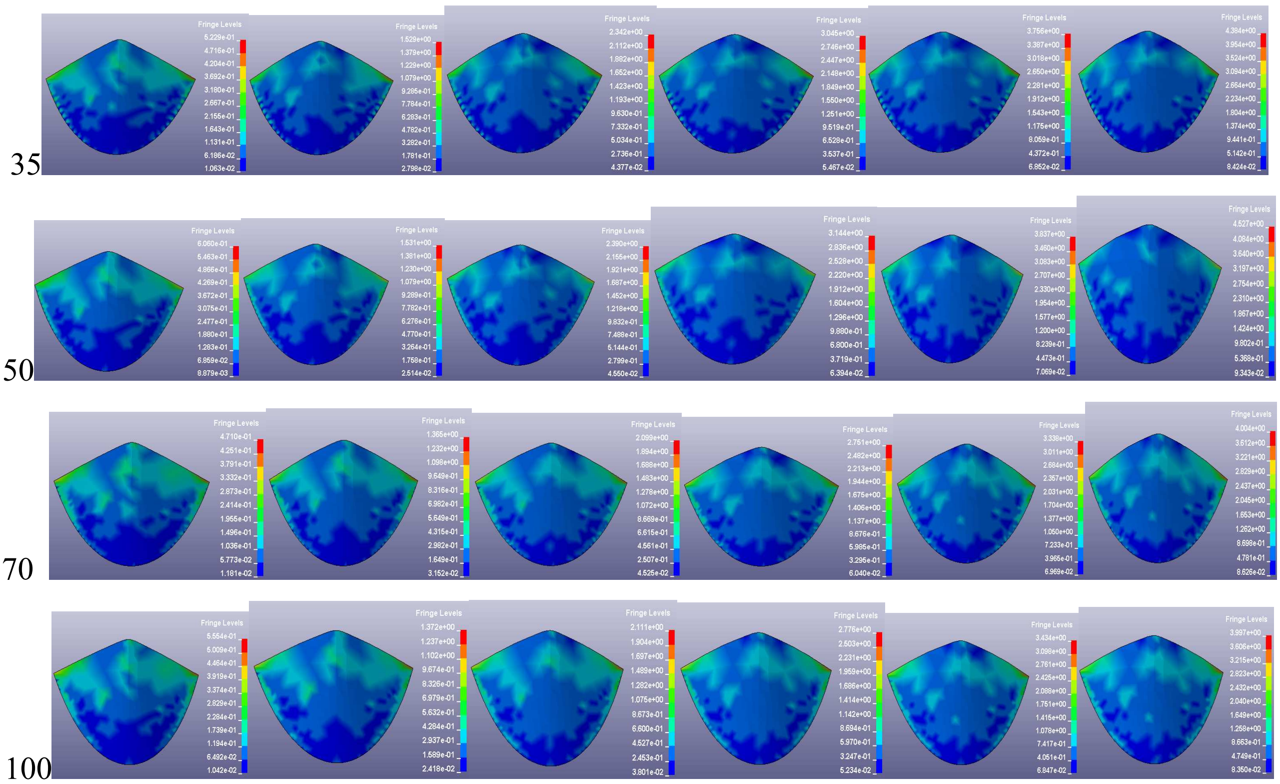

Figure5. Stress distribution of paraboloidal valve leaflets with different suture density

From the analysis results , we can know that during the loading process, the deformation of valve leaflets are not obvious. The valve leaflets with different suture density did not appear obvious stress concentration area. Uniform stress appears the abdomen of valve leaflets and non-uniform stress appears the edge of valve leaflets. For valve leaflets with 35 and 50 suture density , this kind of phenomenon is more obvious.

Suture points:

35 50

70 100

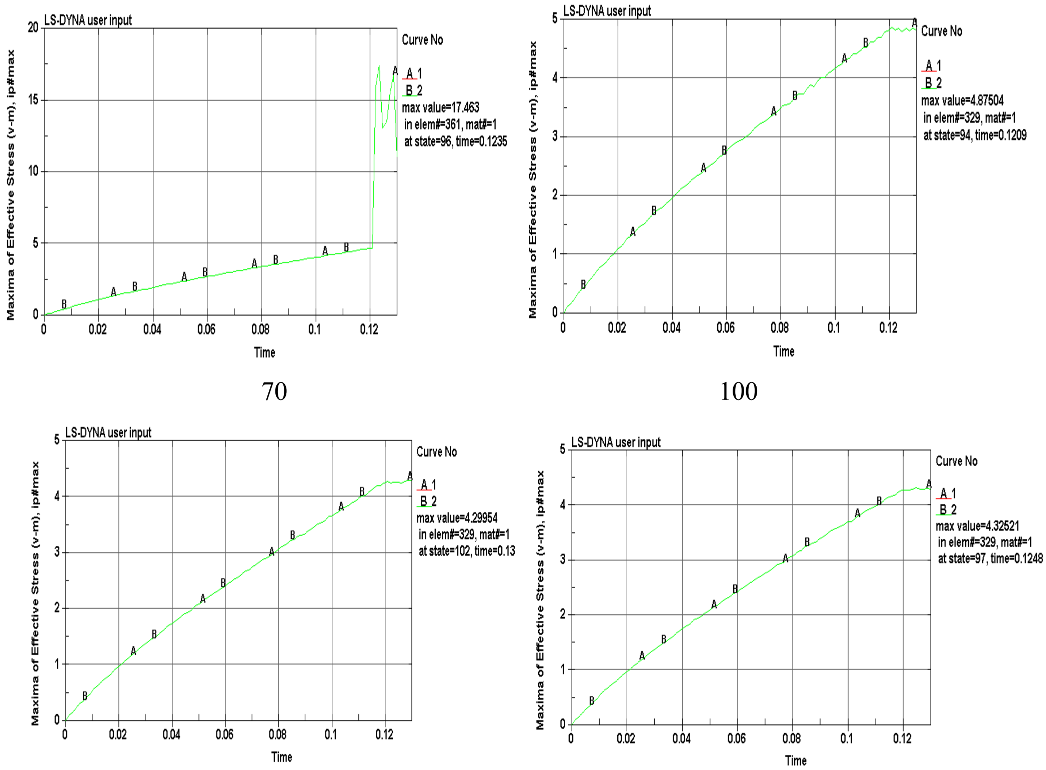

Figure 6. Stress distribution of paraboloidal valve leaflet

From the results, we can conclude that the maximum stress with 35 suture points increases smoothly Within 0-0.12 s, but Within 0.12 s to 0.13 s increases dramatically. The maximum stress of other three kinds of suture density are approximate linear growth over time. The maximum stress with 35, 50 ,70 and100 suture points is 17.46 Mpa , 4.87 Mpa, 4.29 Mpa and 4.32Mpa which all occur within 0.12 s to 0.13 s. Thus we can conclude that this valve leaflet with 70 suture points has better dynamic properties.

Comparison. The dynamic mechanical performance of paraboloidal and ellipsoidal valve leaflet with 50 suture points are better than the paraboloidal and ellipsoidal valve leaflet with 35,70 and 100 suture points.

Paraboloidal valve leaflet with 50 suture points is more appropriate. The stress concentration appears at the top of the attachment edge of all valve leaflets ,and the deformation of this parts are also bigger. From the Stress changing with time curve, valve leaflets all present the approximate linear growth under the suitable suture density. The maximum stress all occur within 0.12 s to 0.13 s. We can find that the dynamic mechanical performance of ellipsoidal valve leaflet with 50 suture points is better than the paraboloidal valve leaflet with 50 suture points.

Summary

This paper constructs the parametric model of the spherical and cylindric heart valve via computer aided design and the dynamic properties of the valve leaflet with different suture density is analyzed using the finite element method. The analysis results are compared and clearly show that the suture density has a significant effect on the mechanical properties of the valve leaflets. The peak von-Mises of the leaflet with different suture density is quite different.This work is helpful to optimize the value of the suture points and prolong the lifetime of the bioprosthetic heart valve.

Acknowledgment

This work was supported by grants from Natural Science Foundation of State (No: 31170906) and Key Laboratory of High Efficiency and Clean Mechanical Manufacture (Shandong University)Ministry of Education.

References

[1] Zhao Shixiong, Luo Zhengxiang.The statue of arificial heart valve [J], Journal of Biomechnical Engineering, vol.8, pp.277-286, 1991.

[2] I.Vesely, The evolution of bioprosthetic heart valve design and its impact on durability, Cardiovascular Pathology, vol.12, pp.277-286, 2003.

[3] Yuan Q., Zhang C. R., Wang X. W., Geometrical design and finite element analysis on the bioprosthetic heart valve. Int J Innov Comput I, vol.3, pp. 1289-1299, 2007.

[4] Cox M. A. J., Driessen N. J. B., Boerboorn R. A., Bouten C. V. C., Baaijens F. P. T., Mechanical characterization of anisotropic planar biological soft tissues using finite indentation: Experimental feasibility. J Biomech, vol.41, pp.422-429, 2008.

[5] Pibarot P. and Dumesnil J. G., Patient-prosthesis mismatch and the predictive use of indexed effective orifice area: is it relevant?, Cardiac Surgery Today, vol.2, pp.43-51, 2003.

[6] G.Arcidiacono;A.Corvi;T.Severi;Journal of Biomechanics;38(2005)

Applied Mechanics and Materials *Online: 2013-09-11*
ISSN: 1662-7482, Vol. 421, pp 29-33
doi:10.4028/www.scientific.net/AMM.421.29

Effects of Knife Shapes and Cutting Speeds of a Mower on the Percentage Pulverization of Sweet Potato Vine

Amer N. N. Kakahy[1,a], D. Ahmad[1,b], MD. Akhir[2,c], S. Sulaiman[3,d] , Ishak A.[4,e]

[1]Department of Biological and Agricultural Engineering, Faculty of Engineering, University Putra Malaysia, 43400 UPM, Serdang, Selangor, Malaysia.

[2]Mechanization and Automation Research Center, MARDI, Serdang, Selangor, Malaysia.

[3] Department of Mechanical and Manufacturing Engineering, University Putra Malaysia.

[4] Department of Electrical and Electronics Engineering, University Putra Malaysia.

E-mail: [a] amer_kakahy@yahoo.com, [b] desa@eng.upm.edu.my , [c] mdakhir@mardi.gov.my , [d] suddin@eng.upm.edu.my , [e] ishak@eng.upm.edu.my

Keywords: Cutting, Knife shapes, Mower, Pulverization, Slasher, Speed, Sweet potato

Abstract . The effects of a rotary slasher with two different shapes of knives (L and Y-shaped) at three cutting speeds (1830, 2066 and 2044 rpm) were studied on percentage of pulverization of sweet potato vine passing through the sieve (< 28 mm^2). The results showed that all the treatments were significant at $p < 0.05$ and $p < 0.01$ significance level. The best result was by Y-shaped knife with highest vine pulverized percentage of 82.76 % and a mower speed of 2440 rpm had the finest vine pulverized percentage of 90.48 %. The best performance for interaction effects between knife shapes and speeds of mower was achieved by the Y-shaped knife and a mower speed of 2440 rpm resulting in an average percentage of 92.62 % of pulverized vine.

Introduction

Previous studies [1] have shown that cutting speed and blade configurations play a critical role in crop harvesting. A study conducted by [2] indicated that the type of mower used can affect turfgrass quality. The mowing performances of rotary and flail mowers were compared Turfgrass quality at a 33 mm cutting height was better with the flail mower than with the rotary mower. No improvement in turf quality was seen with experimental T-shaped knives compared with Y-shaped knives. The flail knives tended to pull up a few thatch while mowing. Different types of mowers and knives were used to cut the vines and leaves and concluded that the type and vertical type mowers sweeping is most effective in the removal of vegetation. Cutting and grass cutting has many variables that have an impact on crushing and some of the important variables are the cutting speed and the percentage of moisture from the vine, and there is a need to establish a model of cutting mechanics and to relate knife parameters to forage material properties [3-6].

In both laboratory tests on single stalks and field experiments on mowers, the evidence suggests that a high impact velocity is required. Typical velocities employed by disc and rotary mowers are in the range 71 - 84 m/s [4]. Study by [7] indicated that in practice two to three times greater than the critical speed may be required when cutting upright single stems. Flail-type machines employ high speed rotating knives about a horizontal axis which cut the standing crop by impact [8]. Chattopadhyay and Pandey [9] stated that flail-type cutting devices require a minimum knife speed for effective cutting.There are requirements for additional cutting mechanics and for further studies of the cutting action of knives and therefore there is a need to create a model of cutting mechanics and to relate knife parameters to forage material properties [10 , 11].

This paper describes the effects of two different knife shapes and three different speeds of a mower knife on sweet potato vine slashing (pulverizing).

Methods

The study was conducted at the Department of Biological and Agricultural Engineering Laboratory, Faculty of Engineering, University Putra Malaysia, to investigate the effects of two different knife shapes (L-shaped and Y-shaped knives) and three different speeds (1830, 2066 and 2440 rpm) of a mower knife on sweet potato vine slashing (pulverizing), at 36.15 % moisture content, wet base (w.b%).

Data were analyzed statistically using ANOVA and the least significant difference LSD calculated at 5 % and 1 % to estimate the differences between the averages, by using the statistical analysis systems (SAS 9.2) 2010 software.

Results and Discussion

Results of the study as shown in Tables 1 and 2 and Figs 1, 2, 3 and 4 show that all the treatments had significant effects on the percentage of vine passing through the sieve (< 28 mm2) at $p < 0.05$. and $p < 0.01$.The best result was recorded from Y-shaped knife with highest vine pulverized percentage of 82.76 % and a mower speed of 2440 rpm had the finest vine pulverized percentage of 90.48 % at $p < 0.01$. The lowest percentage of the pulverization of 76.87 % was for the L-shaped knife.

Meanwhile, the best results for interaction effect between knife shapes and speed of mower was achieved by the Y-shaped knife and a mower speed of 2440 rpm resulting in an average percentage of 92.62 % of pulverized vine passing through the sieve (< 28 mm2) at $p < 0.05$.

These results agree with the findings of [2] who indicated that the performances of mowing was better with the flail mower than with the rotary mower. The results are also in agreement with the findings of [3 , 5 , 6] which showed that all studied treatments had significant effects on the percentage of vine pulverization.

Table 1 Analysis of variance (ANOVA)

Source of variation (S.O.V)	Degree of freedom (d.f)	Percentage of sweet potato vine passing through the sieve (< 28 mm^2) %
Duplicates	2	
Shapes of knife (Sh)	1	156.10042**
Cutting speed (s)	2	553.94708**
Interaction between (Sh × s)	2	8.6191416*
Experimental error	10	1.3081338
Total	17	
		L.S.D 1 %=2.58118 L.S.D 5 %=1.69215

**significant at level 1 %, *significant at level 5 %,

Table 2 Factors influencing the percentage of sweet potato vine passing through the sieve (< 28 mm$^{2)}$%

Sh/s	s1 1830 [rpm]	s2 2066 [rpm]	s3 2440 [rpm]	Mean-Sh
L-shaped (Sh1)	67.52	74.74	88.34	76.87
Y-shaped (Sh2)	76.16	79.49	92.62	82.76
Mean-s	71.84	77.12	90.48	

Sh = shapes of the knife, s = speed of the mower (rpm).

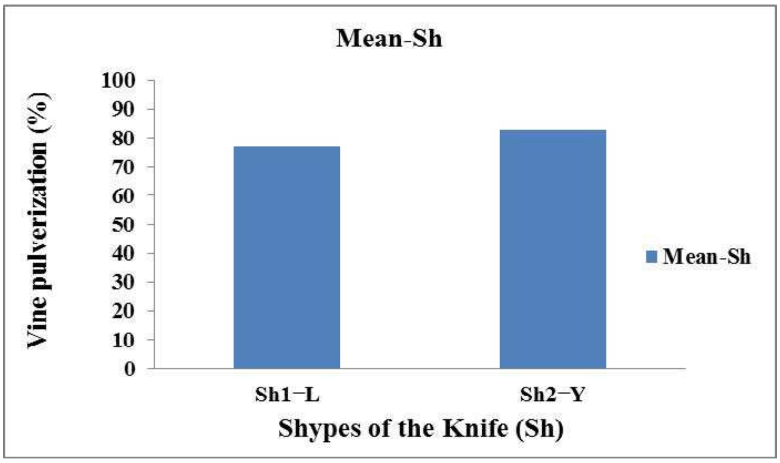

Figure 1 Effects knife shapes on the sweet potato vine passing through the sieve (< 28 mm^2) %.

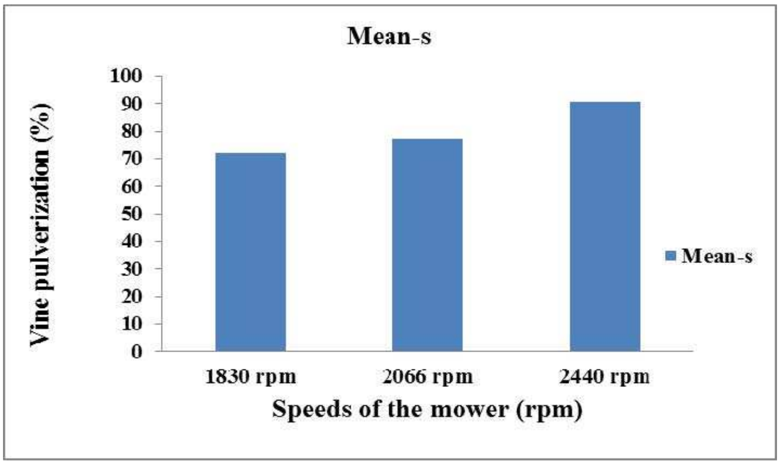

Figure 2 Effects of mower speeds on the sweet potato vine passing through the sieve (< 28 mm^2) %.

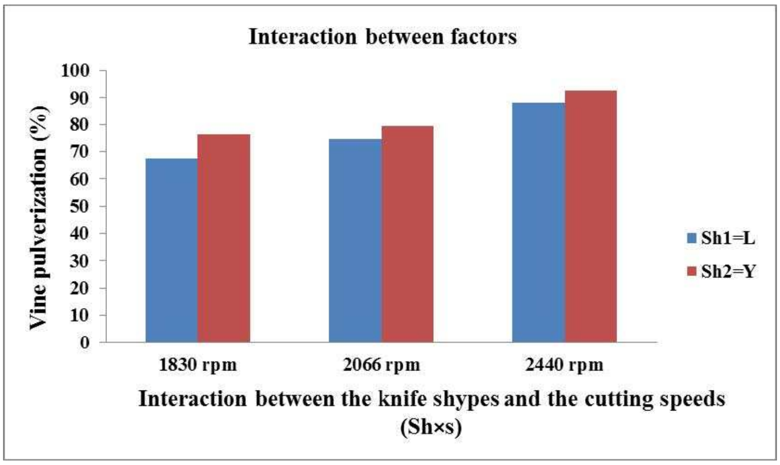

Figure 3 Effects of interaction between the knife shapes and the cutting speeds on the sweet potato vine passing through the sieve (< 28 mm^2) %.

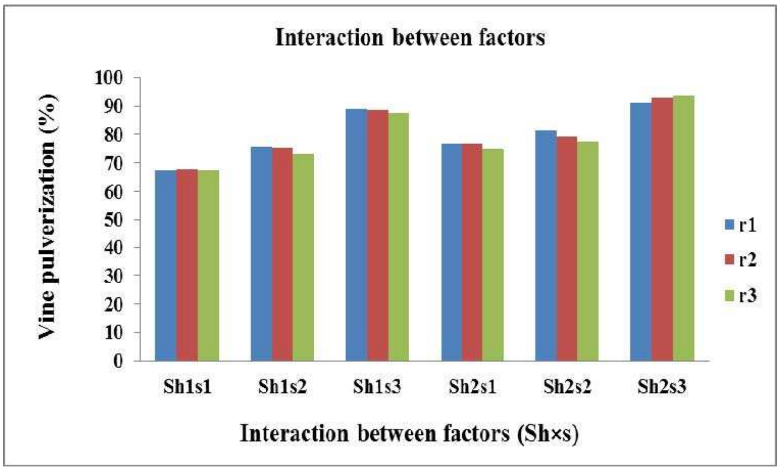

Figure 4 Effects of the treatments on the sweet potato vine passing through the sieve (< 28 mm^2) %.

Conclusion

The study indicated that the best result was for the Y-shaped knife with the highest mower speed (2440 rpm) to have the best value of the percentage of sweet potato vine passing through the sieve (< 28 mm2) of 92.62 %., and there was significant difference of all the studied characters at $p < 0.05$. and $p < 0.01$.

Acknowledgements

Thanks are due to the staff of Agricultural Mechanization and Automation Center, MARDI especially to Mr. Othman Omer Jena senior technician, research assistance M.V. for their generous help and advice during the preparation of this paper. Special thanks for Mr. Hairul Anuar b. Abd Mubin (technician) and Zainal Abidin b. Abdul Ghani (assistant engineer), in the Department of Biological and Agricultural Engineering, Faculty of Engineering, University Putra Malaysia.

References

[1] D. M. Justin, K. M. Sunil, M. F. Brian, E. G. Tony, and C. H. Alan, "Impact of Cutting Speed, Blade Type, and Blade Angle on Miscanthus Harvesting Energy Requirement.," *American Society of Agricultural and Biological Engineers (ASABE).* vol. 12-1338182, 2012.

[2] R. L. Parish and J. D. Fry, "Technical Notes: Mower Effects on Turfgrass Quality," *American Society of Agricultural Engineers.,* vol. 13, pp. 715-717, 1997.

[3] A. N. N. Kakahy, D. Ahmad, M. Akhir, A. Ishak, and S. Sulaiman, "Design and development of an integrated slasher (pulverizer) for sweet potato harvester: A Review " in *1st International Conference in Mechanical Engineering Research (ICMER 2011)*, 2011.

[4] M. J. O'Dogherty, "A review of research on forage chopping," *Journal of Agricultural Engineering Research,* vol. 27, pp. 267-289, 1982.

[5] A. N. N. Kakahy, D. Ahmad, M. Akhir, S. Sulaiman, A. Ishak, and H. Ali, "Effects of Types of Slashers and Cutting Speeds on the Quality of Grass Chopping (Pulverizing) at High Moisture Content," in *International Conference on Mechanical Engineering and Advanced Technology (ICMEAT2012)*, Iran, Isfahan, 2012.

[6] A. N. N. Kakahy, D. Ahmad, M. Akhir, S. Sulaiman, and A. Ishak, "Effects of Types of Slashers and Speeds on Grass Chopping (Pulverizing)," presented at the 2nd Malaysian International Conference on Trends in Bioprocess Engineering (MICOTriBE 2012), Langkawi, Malaysia, 2012.

[7] M. J. O'Dogherty and G. E. Gale, "Laboratory studies of the effect of blade parameters and stem configuration on the dynamics of cutting grass," *Journal of Agricultural Engineering Research,* vol. 49, pp. 99-111, 1991.

[8] P. S. Chattopadhyay and K. P. Pandey, "Effect of Knife and Operational Parameters on Energy Requirement in Flail Forage Harvesting," *Journal of Agricultural Engineering Research,* vol. 73, pp. 3-12, 1999.

[9] P. S. Chattopadhyay and K. P. Pandey, "PM—Power and Machinery: Impact Cutting Behaviour of Sorghum Stalk using a Flail-Cutter—a Mathematical Model and its Experimental Verification," *Journal of Agricultural Engineering Research,* vol. 78, pp. 369-376, 2001.

[10] M. J. O'Dogherty, "Chop length distributions from forage harvesters and a simulation model of chopping," *Journal of Agricultural Engineering Research,* vol. 30, pp. 165-173, 1984.

[11] M. J. O'Dogherty and G. E. Gale, "Laboratory studies of the cutting of grass stems," *Journal of Agricultural Engineering Research,* vol. 35, pp. 115-129, 1986.

Applied Mechanics and Materials *Online: 2013-09-11*
ISSN: 1662-7482, Vol. 421, pp 34-39
doi:10.4028/www.scientific.net/AMM.421.34

Electromagnetic and Vibration Analysis of in-Wheel Switched Reluctance Motor with Notches and Projections for Electric Vehicle Applications

G.Nalina Shini[1], Dr.V.Kamaraj [2], E.Giridharan[3], S.Kannan[4]

[1]Associate professor, EIE, R.M.D. Engineering College, Chennai, India

[2]Professor, EEE, S.S.N.College of Engineering, Chennai, India

[3]Sri Sai Ram Engineering College,Chennai, India

[4] Green energy Technologies, Chennai, India

Email: nalina_arvind@yahoo.com

Keywords: Modified In-wheel SRM with notches and projections, MagNet, ANSYS 14.0, Modal Analysis, Average Torque.

Abstract. With the demand for fuels to cater the needs of day to day usage of vehicles, the best alternative solution is to use electric vehicles. In-wheel Switched Reluctance Motor(SRM) is the best direct drive motor used in electric vehicles owing to its low cost, simplicity, high torque to inertia ratio. Vibration is a major problem which causes acoustic noise. This paper deals with the design and analysis of In-wheel Switched Reluctance Motor which produces high average torque with low vibration. The above desired performance of In-wheel SRM can be obtained by modifying the stator and rotor pole shapes of In-wheel SRM with notches and projections. Electromagnetic analysis of 3 phase 6/8, 1500 rpm In-wheel SRM is done by FEA based CAD package MagNet. Average torque and Torque ripple is obtained from the static torque characteristics. 3D structural FE analysis is done to obtain the modal frequencies of In-wheel SRM. Ansys 14.0 aids in the Structural FE analysis. The performance of modified In-wheel SRM is compared with the conventional In-wheel SRM. The results conclude that the modified In-wheel SRM is superior than the conventional In-wheel SRM in terms of high average torque and low vibration.

Introduction

Switched Reluctance Motor (SRM) is an electrical machine with high torque at low speed, making it a good candidate for direct driving purpose [1]. SRM has a simple and firm construction with no windings and permanent magnets in the stators and rotors. Due to the geometrical simplicity of SRM, it has a lower cost of manufacturing and maintenance than other types of electrical machine. Furthermore, the driving power converter of SRM has an independent circuit for each phase, which provides the great advantages of inherent fault tolerance and potential for high reliability[2-3]. SRM with exterior rotor is applied for the assembly of In-wheel design, which saves space and provides great flexibility in motion control. In-wheel SRM, employed in electric vehicles suffers from vibration which causes driving discomfort. The vibration being an inherent nature of SRM, is caused by torque ripple. When torque ripple is minimized, vibration caused by the In-wheel SRM will also be reduced. There are two approaches to reduce torque ripple. One of these methods is to modify magnetic design and to change the shape of rotor and stator while the other method is based on switching control [4-5]. It is notable that in electronic control method we have to lose some of the average torque instead of which torque ripple is reduced [6]. In general it can be stated that torque maximization and ripple minimization cannot be achieved simultaneously by electronic control but in the method of shape change, this is possible[7]. The stator and rotor pole tip shapes of the SRM with notches and projections reduces the torque ripple [8].In this paper a new mechanical construction with notches and projections in the stator and rotor poles of In-wheel SRM is proposed.

In this work Electromagnetic analysis of modified In-wheel SRM is done using FEA based CAD package MagNet.Structural vibration analysis using ANSYS 14.0 is capable of predicting the mode shapes and the corresponding natural frequencies of In-wheel SRM.